MINOS-doc-1283-v1

Systematic Uncertainties in the NuMI Beam Flux

Sacha E. Kopp, Žarko Pavlović, Dharmaraj Indurthy
University of Texas at Austin

Abstract

This note presents the study of a number of beam related uncertainties that as an end result cause an error in predicted neutrino flux. We considerd following sources of errors: number of protons on target, misalignement of target hall components, horn current uncertainties, baffle scraping and hadron production uncertainties. In the following sections impact of each of the uncertainties on neutrino flux at the near detector and on far over near ratio is studied.

1 Introduction

The NuMI beam flux is created by the decay of focused pions. To understand the changes in the flux spectrum requires knowing both the energy spectrum of the pions in the beam and also their angular divergence as they enter the decay pipe. Recalling the kinematic relation

$$E_\nu = \frac{0.43 E_\pi}{1 + \gamma^2 \theta^2}$$

The neutrino energy E_ν depends on the pion energy E_π directly and the pion direction indirectly through the decay angle θ which is the angle between the pion direction and the direction for the neutrino to reach the near or far detectors. It will therefore be the subject of the present note to investigate effects which alter the number, energy spectrum, and angular divergence of the pion beam.

It is also important to recall that the beamline effects which alter pion focusing are often calculable as to where they affect the neutrino spectrum. The pions (and kaons) emanating from the target at a polar angle θ satisfy

$$\tan\theta = \frac{r}{z} = \frac{p_T}{p_z}$$

where r is the radius at which the pion enters the horn, z is the distance between the pion creation in the target and the horn (on average $z \sim$60 cm for the LE beam), and p_T and p_z are the pion momenta tranverse to and longitudinal to the beam line. p_T does not scale rapidly for the secondaries produced in proton-nucleus collisions, and in fact $\langle p_T \rangle \sim 250$ MeV/c for pions to get through the horns, so that the pion momentum and angle entering the horn are inversely related:

$$p_z \approx p_T/\theta$$

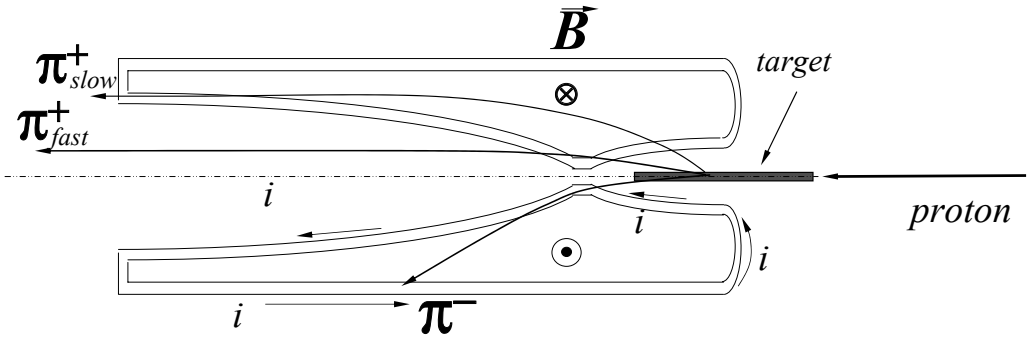

Figure 1: Schematic diagram of a low-momentum pion entering horn 1 at large angle and a fast pion entering the horn at low angle and just grazing the inner conductor.

The relevance of the above discussion is that some effects, such as a horn misalignment, changes the minimum angle θ of pions which receives focusing. Horn 1, for example, has an inner neck of radius 9 mm and is at a distance of $\sim$ 60 cm from the center of the target in the LE position. This suggest that horn 1 focuses particles down to an angle $\tan\theta$=0.9 cm/60 cm $\approx$ 0.02, or a pion momentum as high as $p \approx (250\ \mathrm{MeV})/0.02 = 13\ \mathrm{GeV}/c$, which corresponds to neutrino energies $E_\nu \approx 11\ \mathrm{GeV}/c$. Affects which move the horn focal region, such as a transverse misplacement of the horn, affect its minimum radius of focusing and hence the momentum range of pions which can be focused by the horns.

Figure 1 represents schematically the above discussion. Fast pions exit the target at small angles and can pass through the field-free aperture ("neck") of the horn, while slower pions exit the target at larger angles and enter the horn field region between the two conductors. Figure 2 shows the ND spectrum, broken up into 5 categories of focused pions: (1) very high energy pions pass through the necks of both horns at small angles, contributing to the high energy tail; (2) slightly softer pions exit the target at small enough angle to pass through the neck of horn 1, but are focused by horn 2; (3) the next softest category of pions enters horn 1, is underfocused (*i.e.* is still diverging as it exits horn 1), but is brought into focus by horn 2 (this category constitutes the vast majority of the flux in the LE beam); (4) still softer pions enter horn 1 are soft enough to be brought into focus entirely by horn 1 and pass (parallel) through the (larger) neck of horn 2; and (5) the softest pion momenta contributing to the neutrino flux consists of pions which are actually over-focused by horn 1 and are rescued by horn 2. Figure 3 shows the same breakdown for the pME and pHE beams.

The remainder of this note investigates effects such as horn misalignments and magnetic field modelling which affect the geometric ray tracing of pions through the horns, our knowledge of the precision of the proton beam intensity (which affects the net flux scale), the effects of the proton beam shape on the target, and finally the model of pion yield (hadron production) from the target, which affects significantly the momentum and transverse momentum of pions from the target.

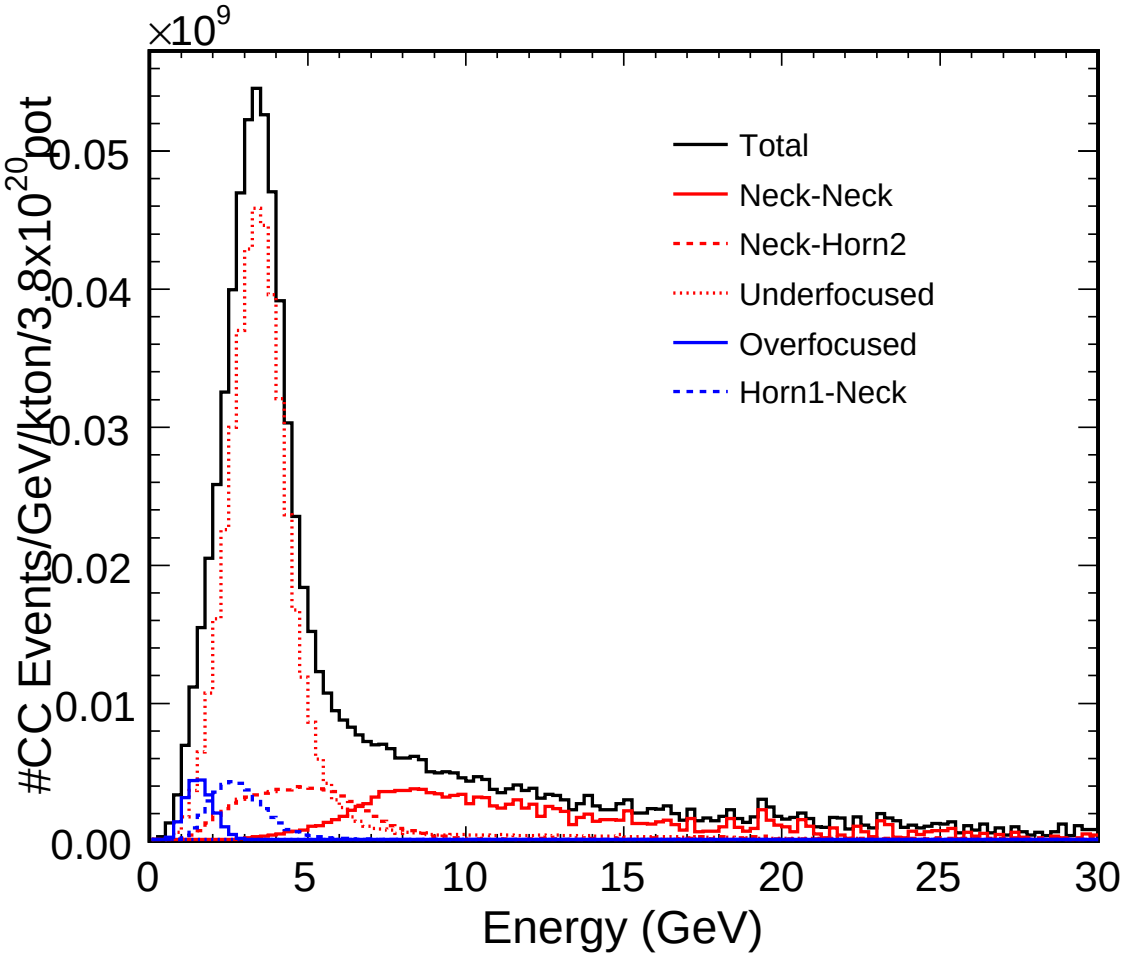

Figure 2: ND neutrino spectrum in the LE10 beam, along with 5 categories of pion trajectories through the horns (see text).

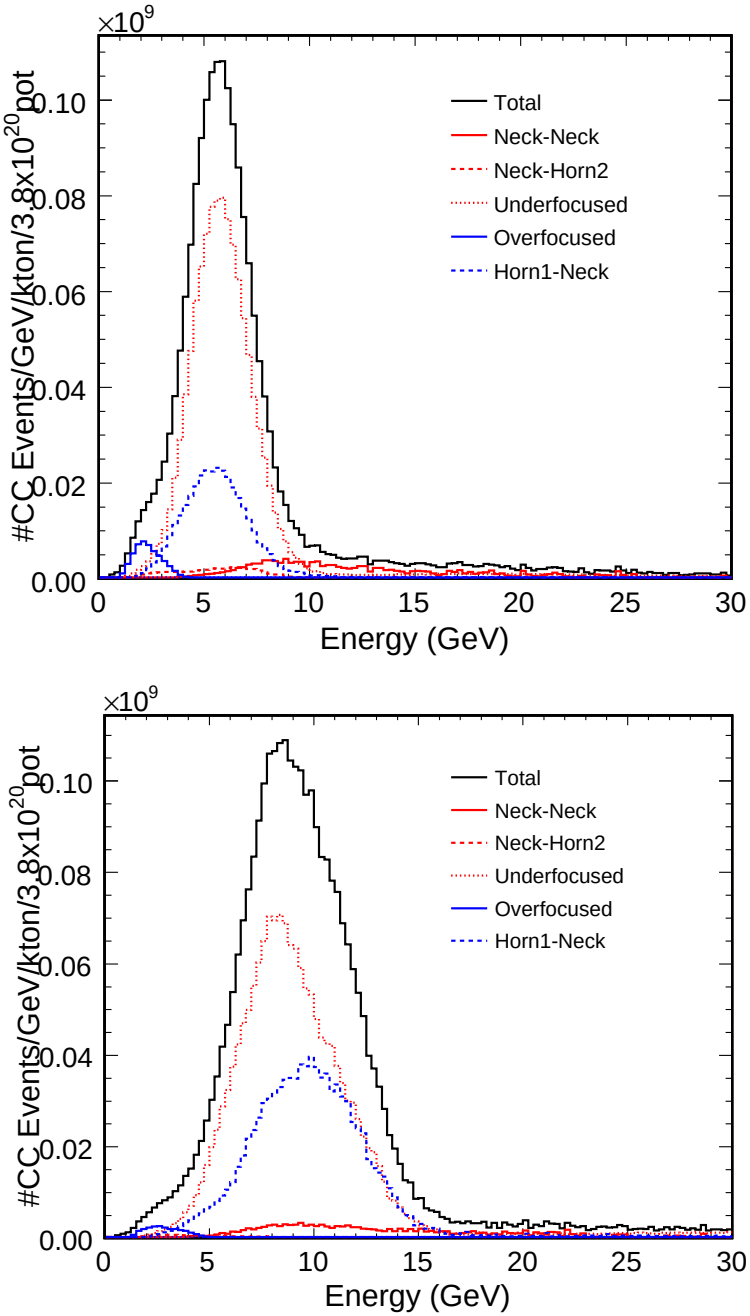

Figure 3: ND neutrino spectrum in the pME(top) and pHE(bottom) beams, along with 5 categories of pion trajectories through the horns (see text).

2 Integrated Proton Intensity

The proton intensity in the NuMI beamline is monitored with two toroids, Tor101 which is at the begining of NuMI beamline and TorTGT which is at the end of the beamline and just before the target. In addition to that data from a toroid in Main Injector called IBEAM is also logged. The NuMI toroids have a 12 and a 14 bit readout, with the 14-bit readouts being labelled TrTGTD and Tr101D. The studies below pertain to the 14-bit readouts. The present note will document the known systematic effects which affect the accuracy and precision of the toroid information. A more comprehensive note is forthcoming [1] which will document the live-time for the toroids' readout and errors due to missing data over the course of the run. The studies mentioned here are based on contributions by Doug Jensen in [1], who has been looking at these effects in detail. The purpose of repeating them here is to confirm the similar observations using the MINOS data stream (to be contrasted with raw ACNET data coming through the data loggers as studied in [2]). The effects affecting the toroid precision and accuracy are:

1. **Calibration Scale**: The toroids have been calibrated absolutely using a precision current source. This effort was conducted by Doug Jensen and Aisha Ibrahim on July XX, 2005. Our overall toroid scale is set by this absolute calibration. As a check of this absolute calibration, the toroids were later compared to the Main Injector DCCT I:BEAM, which has been stated to agree with other toroids in other transfer lines (MI8, antiproton line, P150 line) very well (better than 1%). Figure 4 shows that after the current-calibration, our NuMI toroids agree with the Main Injector DCCT to within $\sim 0.5\%$.

2. **Pulse-to-Pulse Precision**: The precision of the toroids can be studied if we compare the readings of two toroids. How well two toroids track each other can be seen in Figure 5. Difference between the two toroids accross the span of pulses with different intensities is less then 10^{11} protons. Looking at the fractional difference between the two toroids we see that the readout of both toroids is within 0.1%. This tells us that the precision of the two toroids is of that order of magnitude.

3. **Non-linearity**: The nonlinearity of NuMI toroids was checked by comparing them to Main Injector toroid (IBEAM) [1], and also by checking one against the other. The toroids showed slight nonlinearity at low intensities (see Figure 5). Since the vast majority of NuMI spills are at intensities $\sim 2.5 \times 10^{13}$ this nonlinearity effect could contribute of order $0.1{\times}10^{12}$ ppp, or $\pm 0.4\%$, uncertainty to our integrated number of protons on target.

4. **Electronics Drift**: Figure 6 shows the pedestals for the two NuMI toroids (read-out values when there is no beam delivered to NuMI). Pedestals are of the order of 5^9 protons, or of order 0.05%. More significantly, the pedestal is observed to drift by $\sim 4 \times 10^{10}$ protons/pulse over the course of our run, and varies separately for each toroid. Since no effort has been made to do a pedestal subtraction, we must ascribe a

$\pm 0.2\%$ error to the toroid values taken at 2×10^{13} ppp. That this pedestal drift does in fact contribute to a variation in toroid values may be seen in Figure 7, which shows the ratio of Tor101 and TorTGT readings over a period of a month. Indeed, $\sim 0.2\%$ temporal variation is seen.

5. **Electronics Gate**: Figure 7, which was intended to show long-term drift of the Tor101/TorTGT relative calibration, also reveals periodic shifts in this ratio which was traced to different spill length times and their position within the toroids' integrating electronics' gate. The NuMI beam runs in three different modes, NuMI only (either 5 or 6 batches), mixed mode (in which NuMI gets 5 batches and pbar gets one slip-stacked batch) and interleaved mode (in which every other NuMI spill is either run with or without pbar beam; this mode can at various times be 5 or 6 batches for NuMI). Looking at the ratio of TorTGT to Tor101 when running in different modes we see a shift of the order of $\pm 0.2\%$ (see Figures 8-10). Since the effect is connected to the different running modes, it could be due to the beam spill falling within a different portion of the electronics' gate (due to either the delivery of batches 1-5 or 2-6 or the delivery of 5 batch, 8.6 μsec, spills *vs.* 6 batch, ~ 10 μsec, spills).

The above effects indicate uncertainties of order 0.5% (absolute calibration scale), 0.1% (pulse-to-pulse precision from electronics), 0.4% (non-linearity), and 0.2% (electronics gate effects), this suggests that the ultimate toroid uncertainty should be of order 1%. For this first round of analyses, however, the Beam Group is recommending 2% uncertainty. As mentioned previously, a separate paper is being prepared to document how much data is missing due to toroid readout errors, *etc* [1]. The conclusions from that paper are that approximately 1.4% of our data must be thrown away (which is being done by everyone using the beam quality cuts), but that the remaining error due to bookeeping mistakes between the ND or the beam data is far below 0.1%.

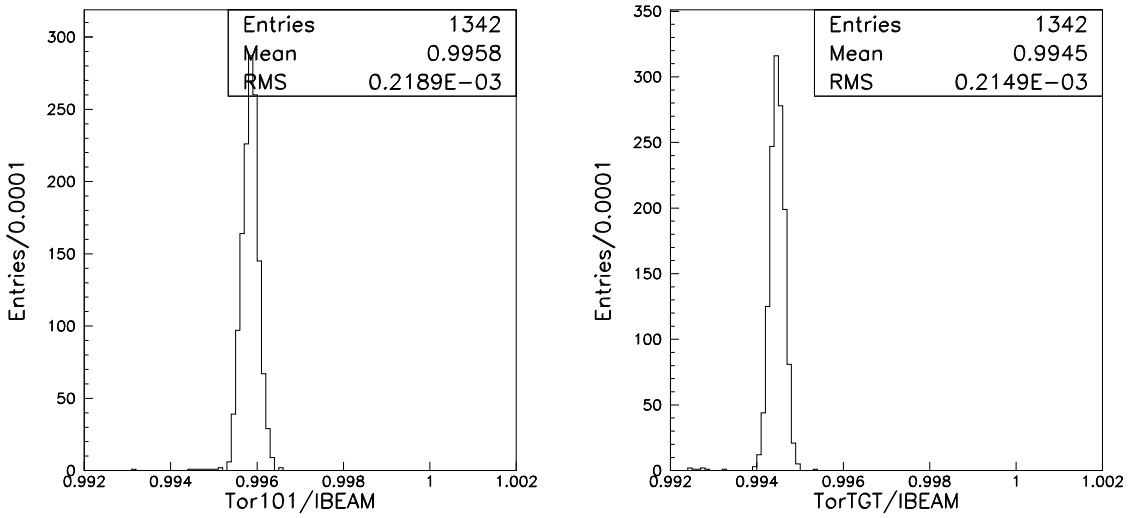

Figure 4: Two NuMI toroids compared to Main Injector Toroid called IBEAM. Shown are the ratios of NuMI toroid currents compared to the I:BEAM current for several NuMI-only accelerator cycles (ie: all the MI beam was delivered to NuMI). Data are from November 11th 2005, after the July XX calibration.

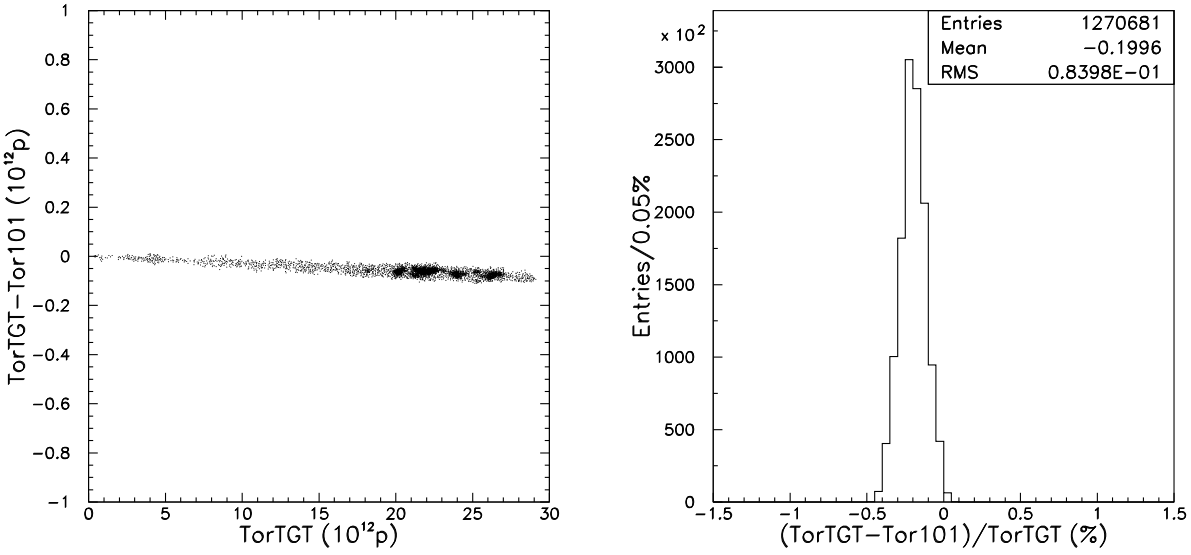

Figure 5: Top plot shows the difference of the two toroids in NuMI beamline (TorTGT and Tor101) versus TorTGT and the bottom plot shows the histogram of fractional differences between the two toroids. The width of the histogram in bottom plot suggests that the precision of the toroids is of the order of 0.1%. (Data from August and September 2005.)

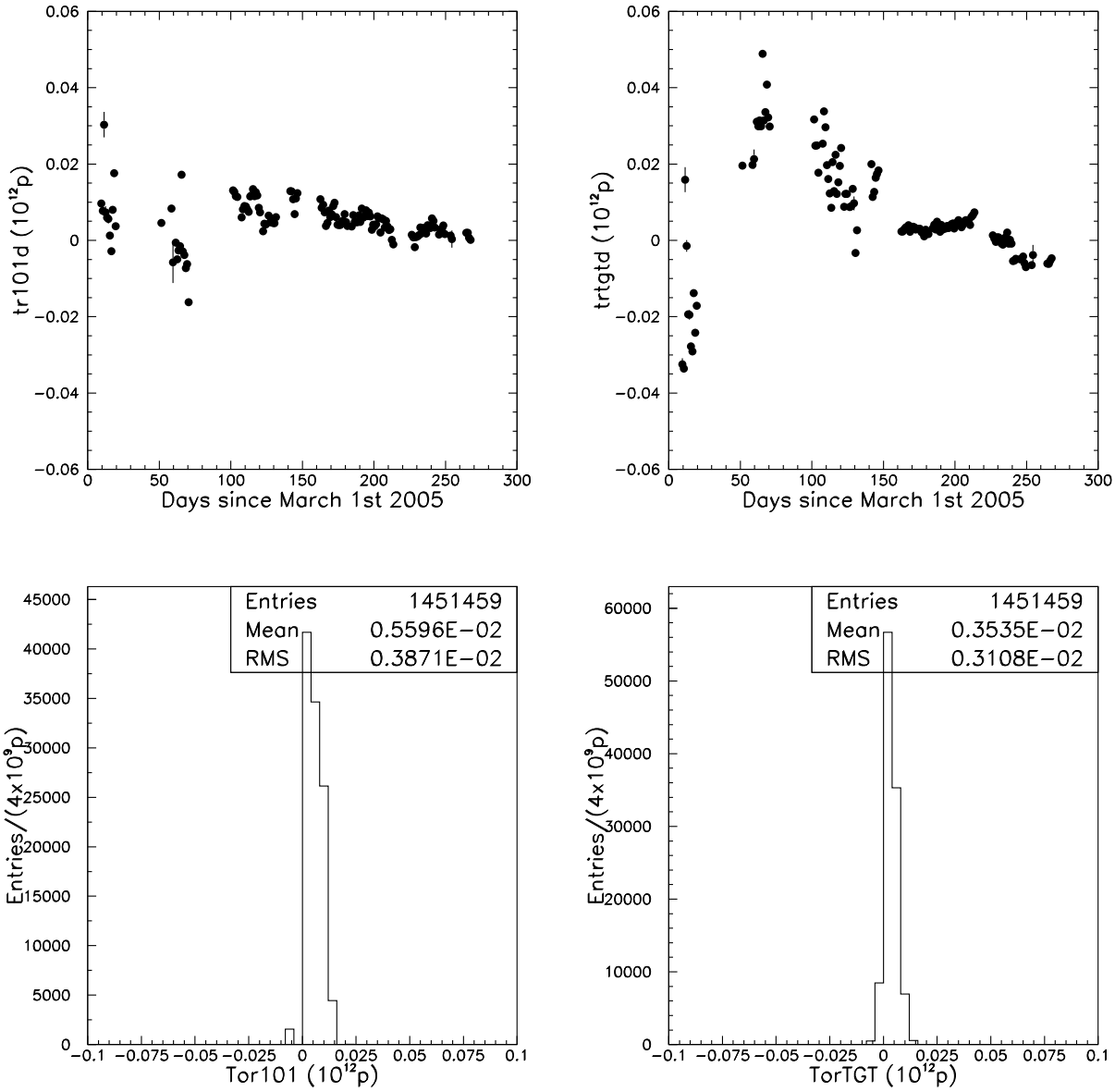

Figure 6: NuMI toroid readout for pulses without beam. Top plots show the readout for a period oof time. Each point corresponds to an average over one day. Bottom plots show histogram of pedestals (data for bottom plots is from August 10. 2005. - September 29. 2005.)

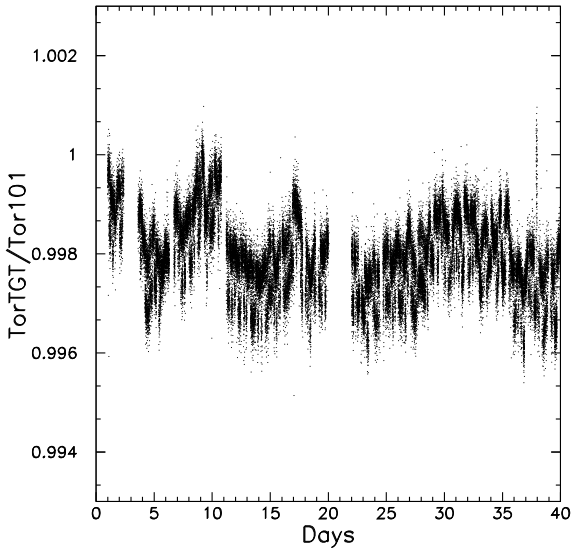

Figure 7: Plot of the ratio of TorTGT to Tor101 plotted over a long period of time (Data from August 10th - September 20th 2005). The drift in this ratio by $\pm 0.2\%$ is similar to the magnitude of the drift observed in the toroids' pedestal values.

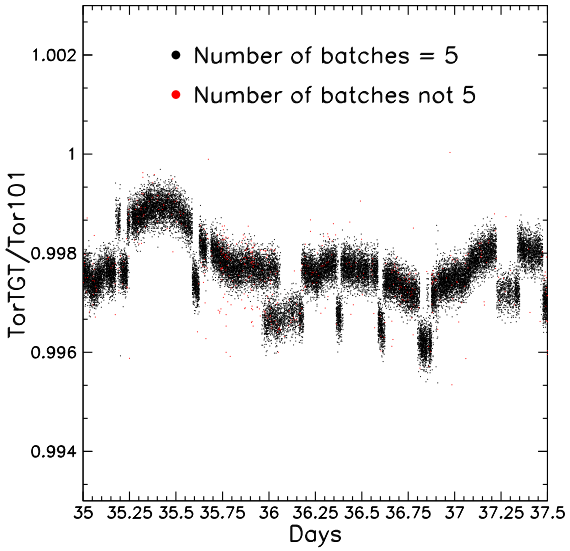

Figure 8: Selected data from Figure 7. The ratio of toroid readouts changes slightly as NuMI transition from mixed-mode, NuMI-only, and interleaved modes.

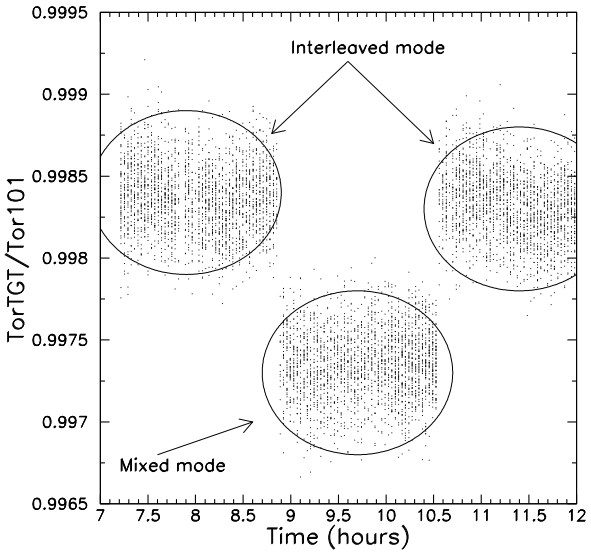

Figure 9: The plot shows how the ratio of TorTGT to Tor101 shifts when NuMI beam is ran in different modes. Number of batches in both modes in this case was 5. Data is from August 17th 2005.

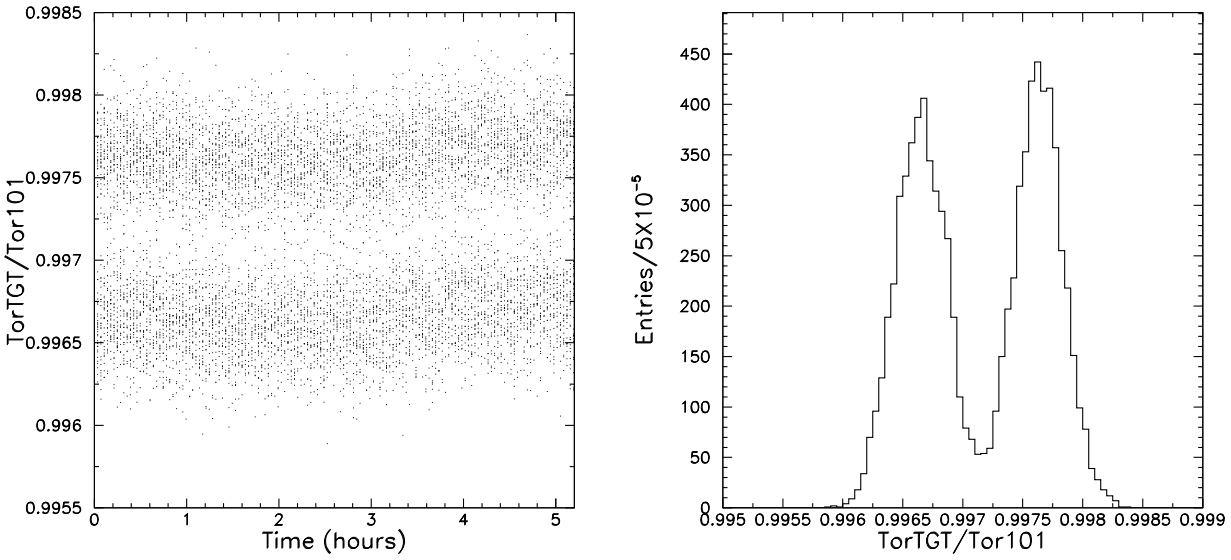

Figure 10: Double-valuedness of one of the NuMI toroids when running in interleaved mode. Left plot shows the ratio of TorTGT to Tor101 versus time for few hours of running in that mode and the right plot shows the histogram of the ratios for the same time period. Data from August 23rd 2005.)

3 Spot Size Effects

The proton beam incident on the target has of order 1.1×1.3 mm^2 sigma. This has several ramifications. First, the spot size is not small compared to the target size, so some beam actually misses the target, reducing the neutrino flux. Second, some fraction of the beam strikes at sufficient distance off-center as to strike the upstream horn-protection baffle, which acts as an additional target. Third, the location of the incident proton affects the creation point of the pions, which in turn affects those pions' probability for re-interaction in the target. We discuss each of these effects in turn.

The spot size at the NuMI target is not exactly measured, since there is a final focusing pair of quadrupoles (Q120 and Q121) which are approximately 20 m upstream of the target. We have two profile monitor SEM's, PM121 and PMTGT at 16 m and 6 m, respectively, upstream of the target. In practice, PM121 is retracted from the beam during most operations to reduce beam loss, and only PMTGT is in place for all beam spills. Thus, while the device resolution on spot size is of order ~ 6 μm [3] for PMTGT, the uncertainty on the spot size at the target is larger because we must rely on knowledge of the beam optics to extrapolate the measured spot size at PMTGT to the target location. To be conservative we take the error in spot size to be $\sim 50 - 100$ μm.

3.1 Beam Fraction Missing Target

The number of protons on target should be corrected downward to account for the number of protons that miss the target. Figure 12 shows the measured horizontal and vertical beam width for $\sim 10^6$ spills as measured by profile monitor SEM PMTGT. On the average beam width is 1.1mm in horizontal direction and 1.2mm in vertical direction. Figure 11 shows one horizontal beam profile at the target; the shaded region of the plot indicates where the horizontal boundaries of the target. The target fins are only 6.4 mm wide in the horizontal plane, so in this plane it is possible for some of the protons to miss the target. Figure 11 also shows a histogram of the fraction of the proton beam missing the target in the horizontal direction for $\sim 10^6$ spills, which has a mean of $\sim 0.2\%$. To be conservative, we take this number to be $(0.5 \pm 0.5)\%$, which we factor into are increased toroid uncertainty of 2%.

3.2 Baffle scraping

The large beam spot size also causes a small fraction of the protons to hit the horn protection baffle which stands in front of the target. The baffle is made out of graphite and acts as another target; since this baffle is further upstream of the real target, it produces a higher energy neutrino beam, as for example we would expect from the variable neutrino beam energy concept [5]. Figure 16, taken from [5] shows the neutrino spectrum for different positions of target. We see that as we pull target further backward we get more high energy neutrinos. Baffle scraping thus adds higher energy neutrinos to the spectrum.

Figure 13 shows one measurement of the profile and the baffle aperture and also the

estimated fraction of the beam on baffle per spill for few months of accumulated data. The mean on this plot is less than 0.15%. We took $(0.25 \pm 0.25)\%$ as a conservative value. .

Figure 14 shows comparison of GNuMI simulation of beam on target and beam on baffle for flux at Near Detector and Far over Near ratio. Figure 15 shows the effect on far over near ratio for different fractions of the beam scraping the baffle. Two different configurations were simulated: one where all protons hit the target and the other where all protons hit the baffle. For the LE beam, the error on the neutrino spectrum and F/N ratio was estimated using these two spectrums, added together to get 0.25% protons on baffle.

For the pME and pHE beams, we used some approximate scaling estimates to derive the ND flux error and the F/N ratio error. For the ND error, we noted that the baffle is approximately 2 m upstream of the actual target (the baffle is 1.5 m long and there is a $\sim$ 60 cm gap between the two. Therefore, the spectrum from the baffle should be similar to simply placing a target 2 m upstream of the pME or pHE target position (this can be verified for the LE beam, since the 1.8 m target position of Figure 16 resembles the baffle spectrum of Figure 13. The baffle is not as efficient at producing neutrinos, as is evident in Figure 13, since it only has an inner edge for pions to escape and pions exiting outward are likely reabsorbed. Therefore, we scaled down the other spectra xxxx

3.3 Thick Target Effects

As noted by measurements in the muon monitors in Ref. [4], there is an interesting change in the neutrino spectrum that results from protons hitting different portions of the target fins. Protons hitting near the edge of the target produce low and high energy pions, however the higher-energy pions are more likely to escape out the side of the target without suffering re-interactions. Protons striking the center of the target produce the same initial spectrum of low and high energy pions, but these particles must pass through larger amounts of graphite in order to escape the target. Therefore, the high energy pions are more likely to re-interact, giving lower energy pions. The relative gain of high energy pions would imply a stiffening of the neutrino spectrum for protons hitting near the edge of the target.

Such a proton beam spot size effect is predicted as well in the beam MC: Figures 17 and 19 show the effect on the ND flux and the F/N ratio as the proton beam width in the horizontal direction is varied. The plots are derived from GNuMI-v.18 with the FLUKA target particles as input, in which the protons at the target were reweighted so as to achieve different effective spot sizes. In the calculation/reweighting, the number of protons falling off the side of the target was kept constant, as was the number of protons hitting the baffle. Only the distribution of those protons actually striking the target was varied. As can be seen, a stiffening of the neutrino spectrum is, in fact, predicted, for larger spot sizes. Figure **??** shows a similar effect as observed in the muon monitors, although the observations there are clearly going to be a convolution of beam missing the target, beam striking the baffle, and the 'thick target effect' noted here.

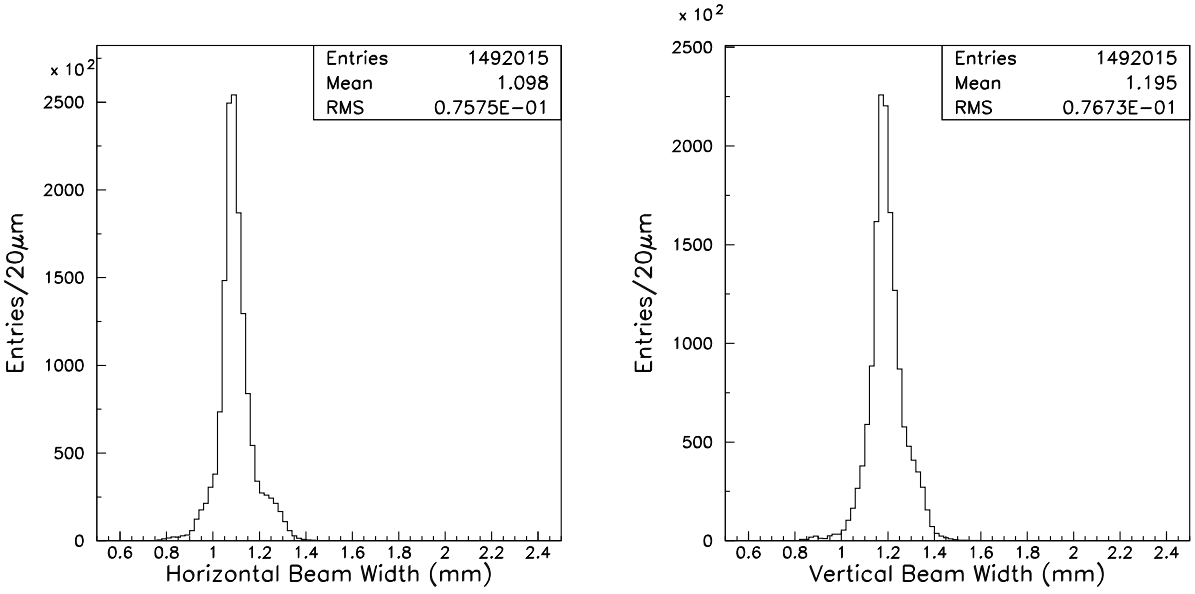

Figure 11: Plots show horizontal and vertical beam width data accumulated over the period of few months. Suggested beam quality cuts are applied.

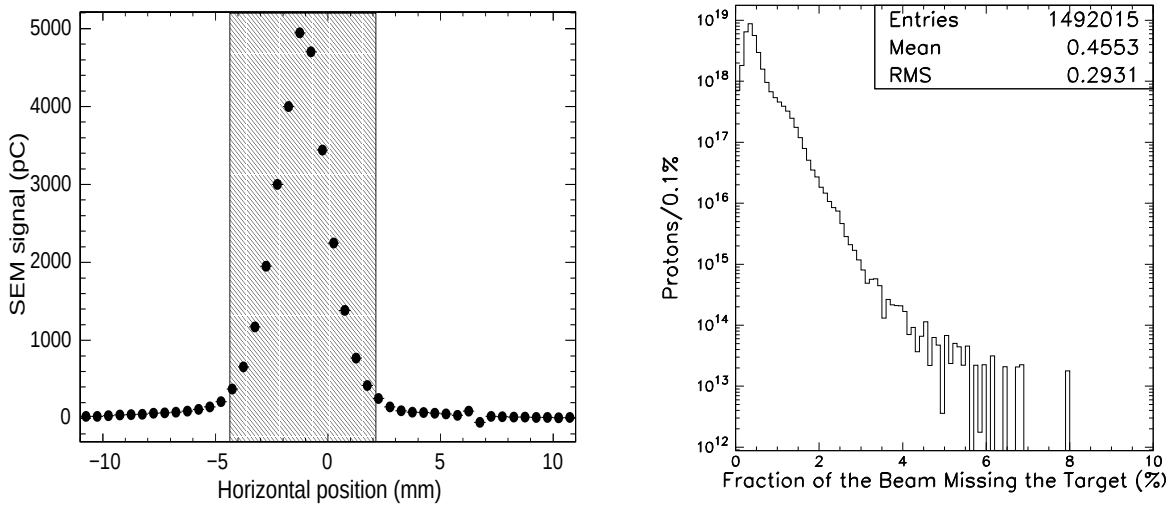

Figure 12: Shaded area on the left plot represents the width of the target and a spill with 1.1mm width is shown. We see that there are some protons missing the target. Right plot shows the fraction of the beam missing the target for the same period of time that was used to make Figure 11.

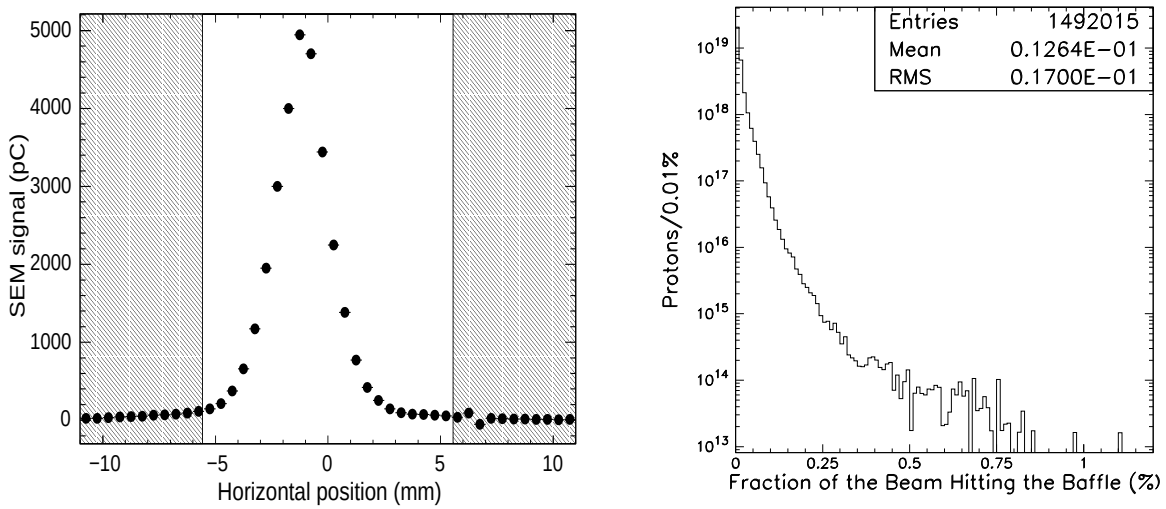

Figure 13: Left plot shows the profile measured by PMTGT of a typical spill. Shaded area shows where the baffle is. Right plot shows the fraction of the beam hitting the baffle.

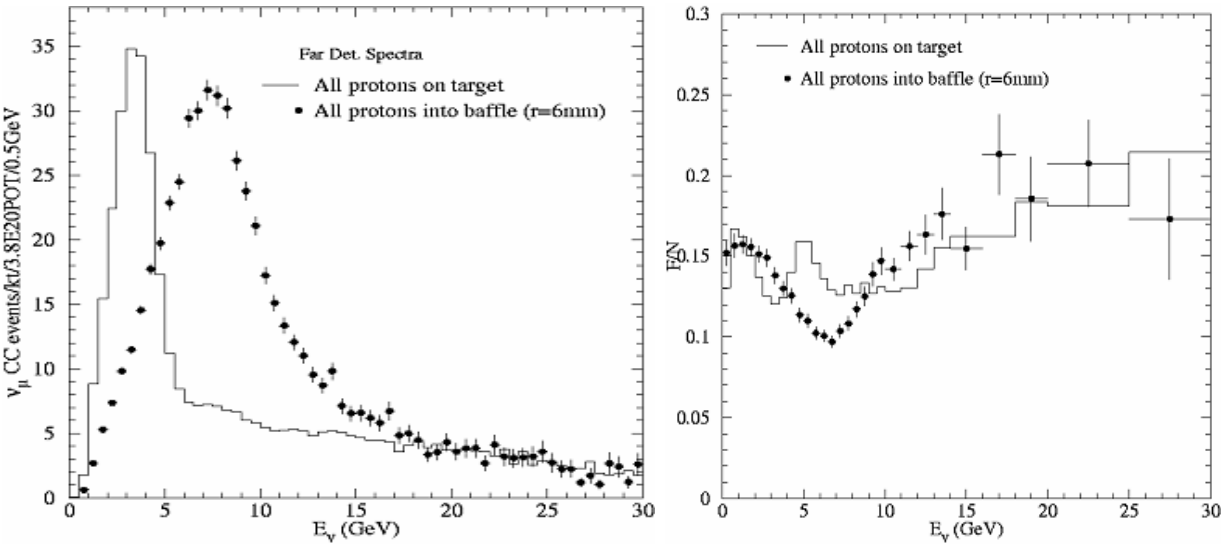

Figure 14: Left plot shows two far detector spectra that correspond to beam on target and beam on baffle. Spectrum shown is for the LE beam. Right plot shows the far over near ratio for those two cases.

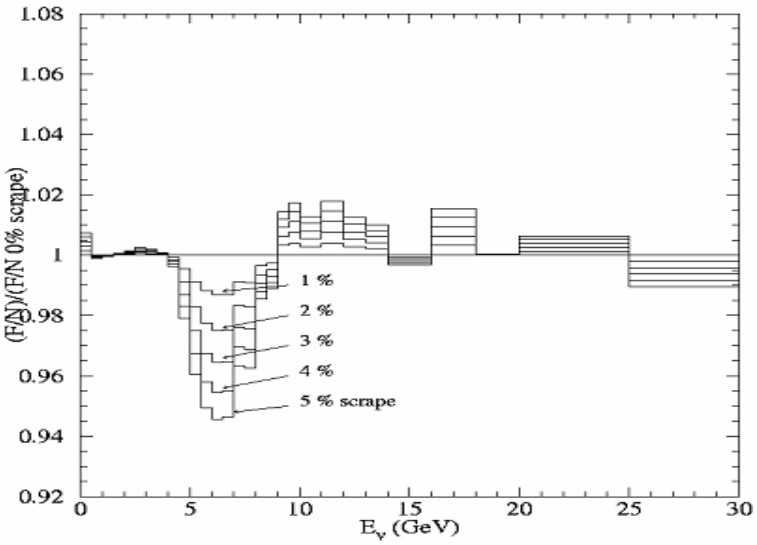

Figure 15: Change in far over near ratio for different levels of baffle scraping.

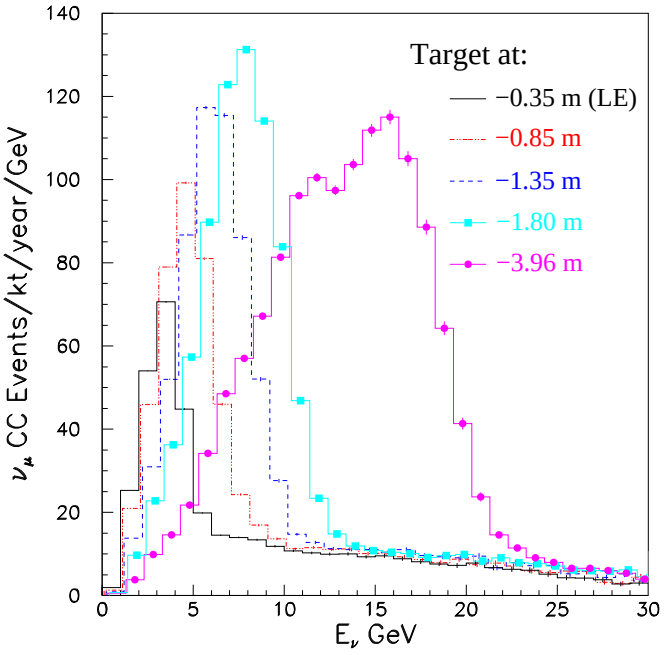

Figure 16: Beam spectrum for different positions of target.

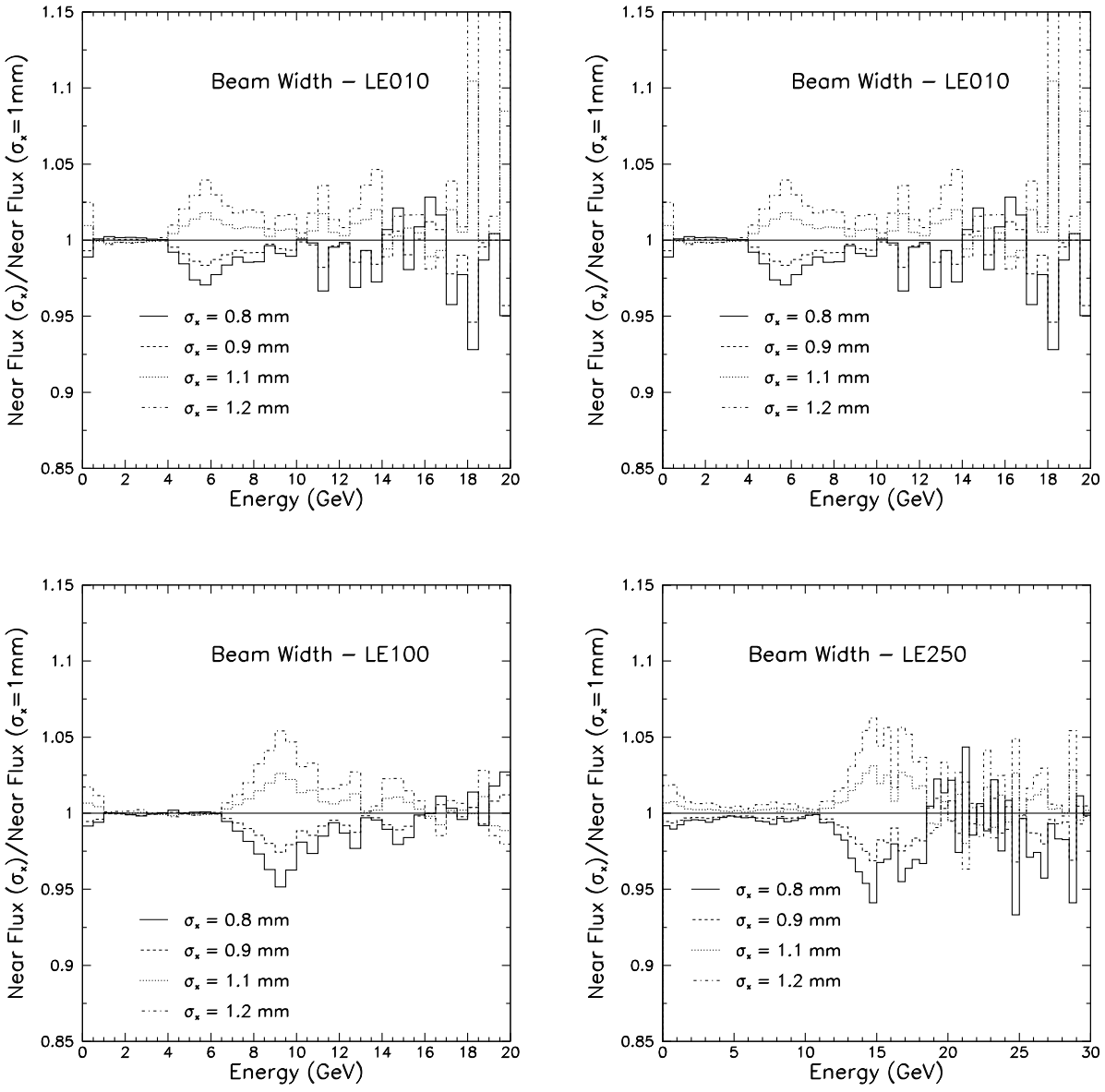

Figure 17: MC calculation of the effect of varying the proton beam spot size on the ND spectrum.

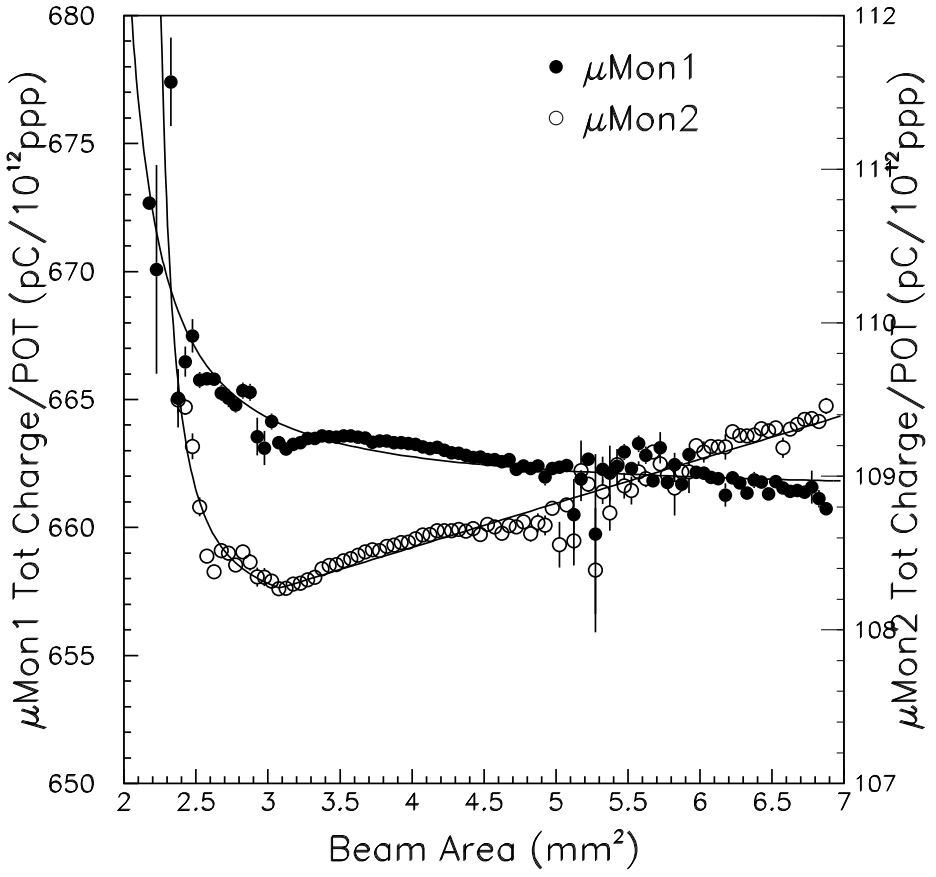

Figure 18: Measured intensity of the muon beam in alcoves 1 and 2 as a function of proton beam area at the target.

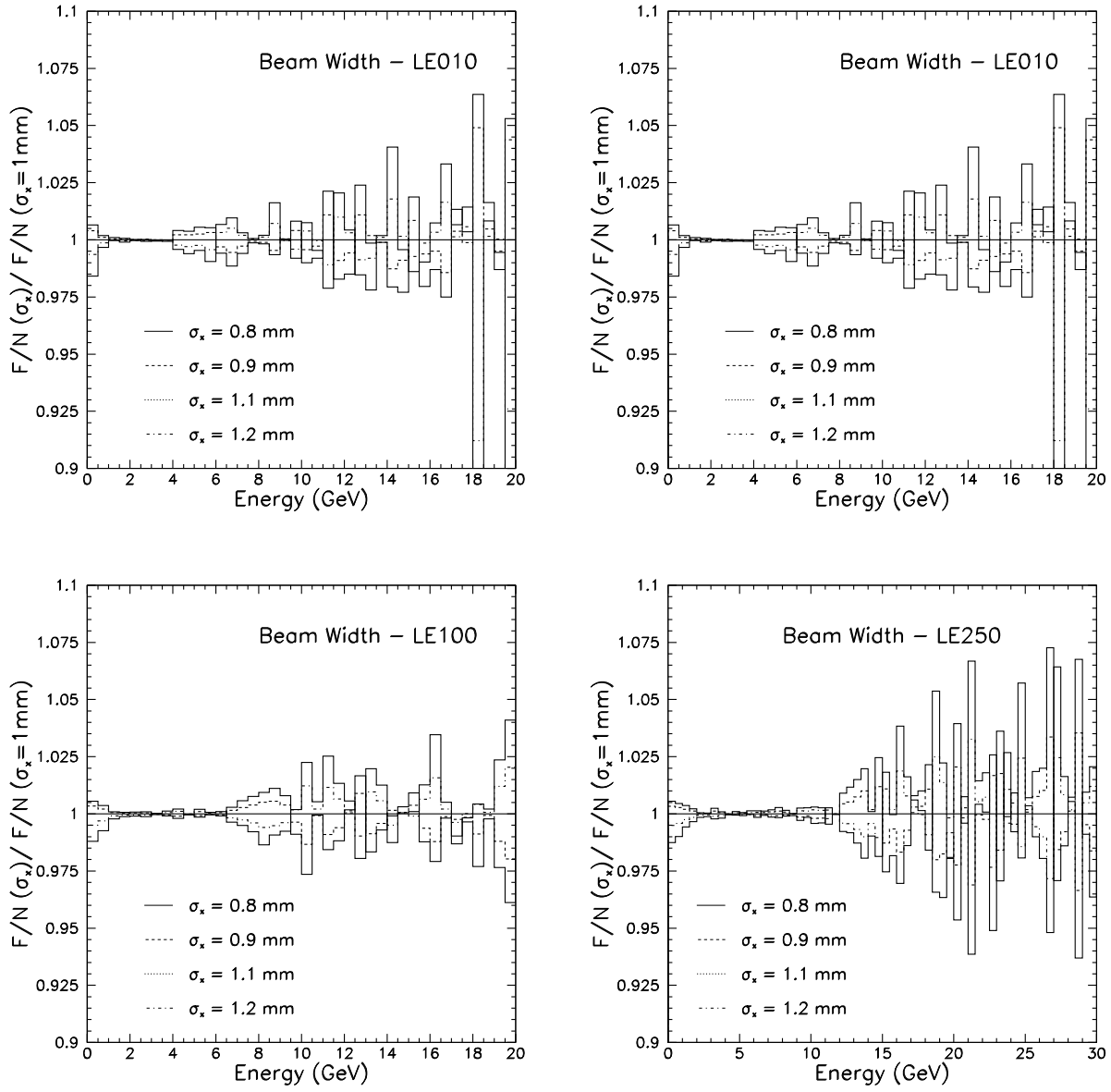

Figure 19: MC calculation of the effect of varying the proton beam spot size on the F/N ratio.

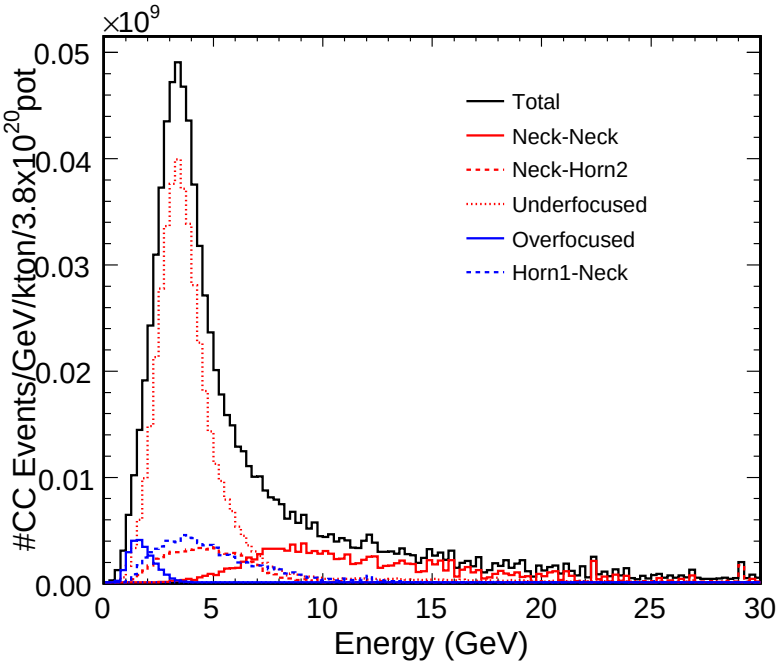

Figure 20: ND neutrino flux calculated with `g4numi` with FLUKA target particles as input. A 4 mm transverse shift of horn 1 was applied, modifying the neutrino spectrum compared with that of Figure 2.

4 Misalignement Errors

Misalignement of some beamline elements causes changes to the neutrino spectrum to change with respect to the nominal spectrum. Some of the elements when moved can affect the flux of pions of certain energy and thus cause the distortion to the spectrum. Figure 1 shows the nominal alignement of the target and the focusing horn. As was noted in Section 1 and indicated schematically in Figure 1, pions at small angles entering the horns contribute to the higher energy portion of the neutrino flux, while wider angle (soft) pions entering the horns contribute primarily to the lower energy portion of the spectrum. Thus, it is our expectation that a horn misalignment, which moves the horn neck further in toward the beam axis, has the effect of increasing the focusing for high energy pions: if the horn is shifted (transverse to the beam) on one side the pions that come at lower angle θ, pions that wouldn't be affected by the horn if it were in the nominal position, will be captured by the horn and on the other side some of the pions that were captured in nominal position, in case with misaligned horn are not captured.

Figure 20, like Figure 2 is again a breakdown of the ND neutrino spectrum into the 5 possible trajectories of pions through the focusing horns. In Figure 20, however, horn 1 has been shifted transverse to the beam line by 4 mm (a somewhat exaggerated amount). Comparison of Figure 20 and Figure 2 reveals that the neutrino spectrum is indeed affected,

and in fact the component most significantly modified are the pion trajectories focused entirely by horn 1.

We considered misalignement of the following beamline elements.

- Horn 1 and Horn 2 offset
- Horn 1 and Horn 2 angle
- Misalignement of the shielding blocks in the chase

PBEAM was used to find the error bar coming from each of the sources. For each beamline element that was studied, five different configurations were simulated, nominal plus four with different misalignements. Nominal here is the configuration that is simulated in gnumi-v18. Ratios of fluxes with misaligned element to nominal flux were then taken. Figure 21 shows the fluxes for different horn 1 offsets and also the ratios of those fluxes to the nominal. Here only 2mm and 4mm offset are shown in the flux plot and all of the simulated configurations are shown in the plot showing the ratios to the nominal flux.

The uncertainty on position and angle of horns we use comes from the results of beam-based alignement of target hall components performed by Bob Zwaska ([4, 8]). The net result of his study was that the horns are shifted 0.5-1.mm with respect to the target and they make angles of 0.1-0.2mrad with respect to the primary beam. In his study the horn position is measured with uncertainty of 0.1-0.3mm. All GNuMI beam MC flux files supplied to the MINOS collaboration have been generated with the horns and target on the nominal beam line axis defined by the primary beam (ie: perfect alignment). Therefore, our procedure in estimating the alignment uncertainty was to take the uncertainty on horn offset to be 1.mm and 0.2mrad on horn angle, equal to the measured offset's in Bob's study.

The alignment effects are noticeable, but relatively small to calculate without significant CPU time. Therefore, an extrapolation procedure was developed: we generated neutrino fluxes for several exaggerated offsets of the horns or targets, offsets larger than expected in the NuMI beam line. An example for horn 1 offsets in the LE10 beam is shown in Figure 21. In each bin of the right plot of this figure, we fitted a second order polynomial of the measured neutrino spectrum distortion as a function of the magnitude of the misalignment. The left plot of Figure 22 shows the result of the fit for two different bins in neutrino energy, namely 4 GeV and 6 GeV. Once the fitted polynomial was found the neutrino flux error was calculated by evaluating the polynomial at the magnitude of 1.0 mm offset, which is what we claim is our alignment uncertainty for now. Repeating this polynomial extrapolation for each bin in neutrino energy, we obtain the expected flux distortion for a 1 mm horn shift, shown in the right hand plot of Figure 21. This was done for the flux at the Near Detector and also for the Far over Near ratio.

Varying the position of the shielding blocks in the chase didn't show any significant change to the flux beyond the statistical fluctuations in the MC. The uncertainty of the block position that was assumed is 10mm.

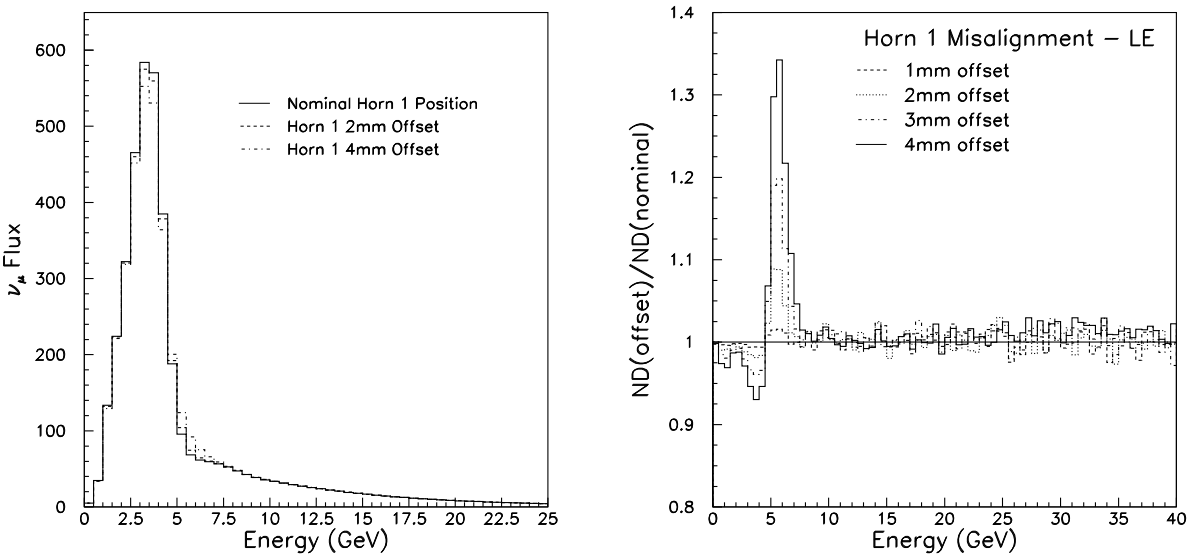

Figure 21: Top plot shows PBEAM fluxes for few different horn 1 offsets and the bottom plot shows the ratios of those fluxes.

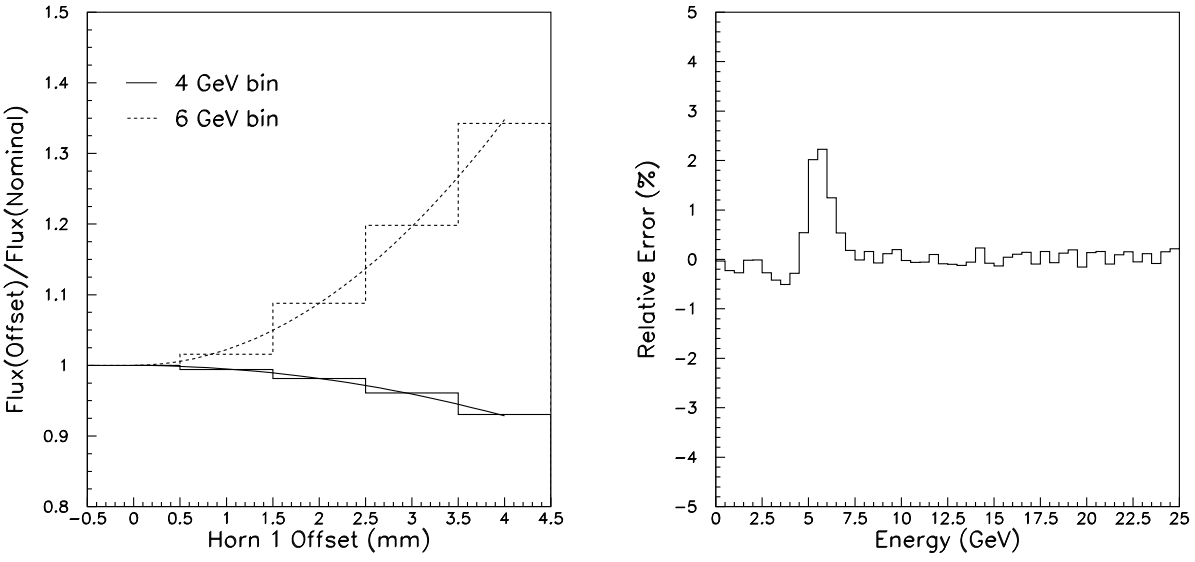

Figure 22: Top plot shows only 4 GeV and 6 GeV bins of Figure 21 ploted versus horn offset and the fits to those bins. Bottom plot shows calculated error bar for horn 1 offset using known uncertainty on the position of the horn and a fit for each bin.

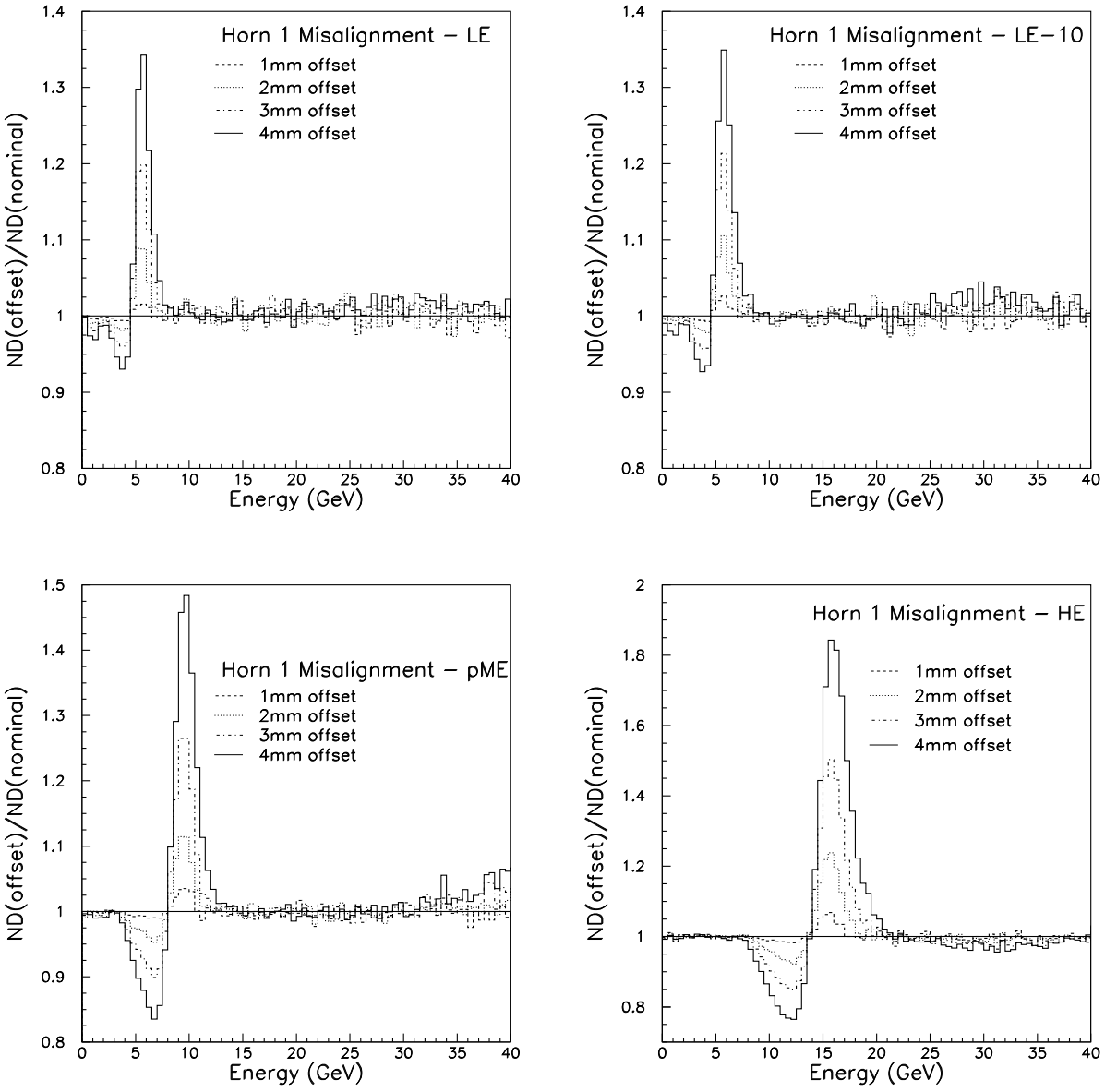

Figure 23: Near Spectrum fractional change due to Horn 1 Offset.

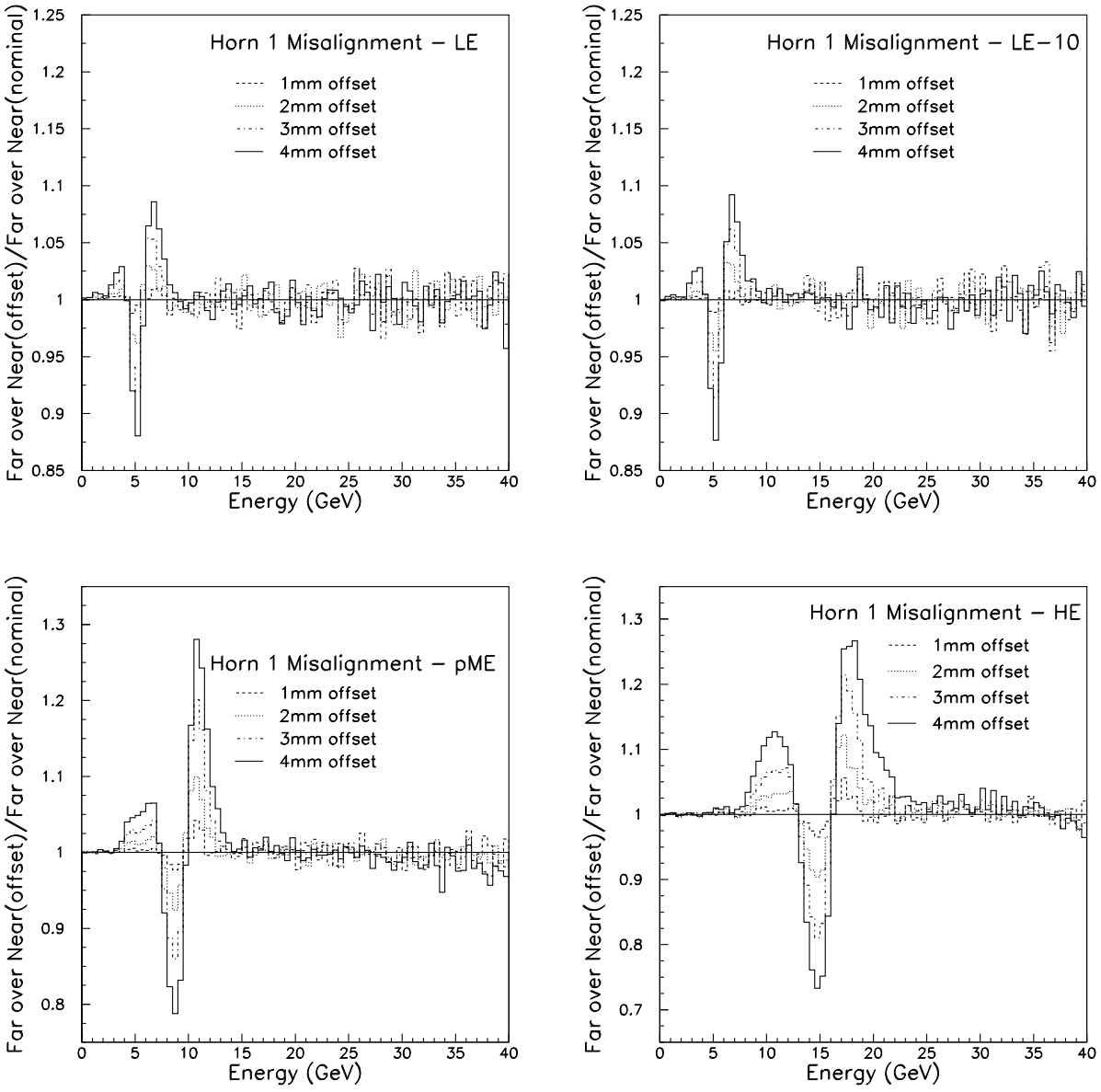

Figure 24: Far over near Ratio fractional change due to Horn 1 Offset.

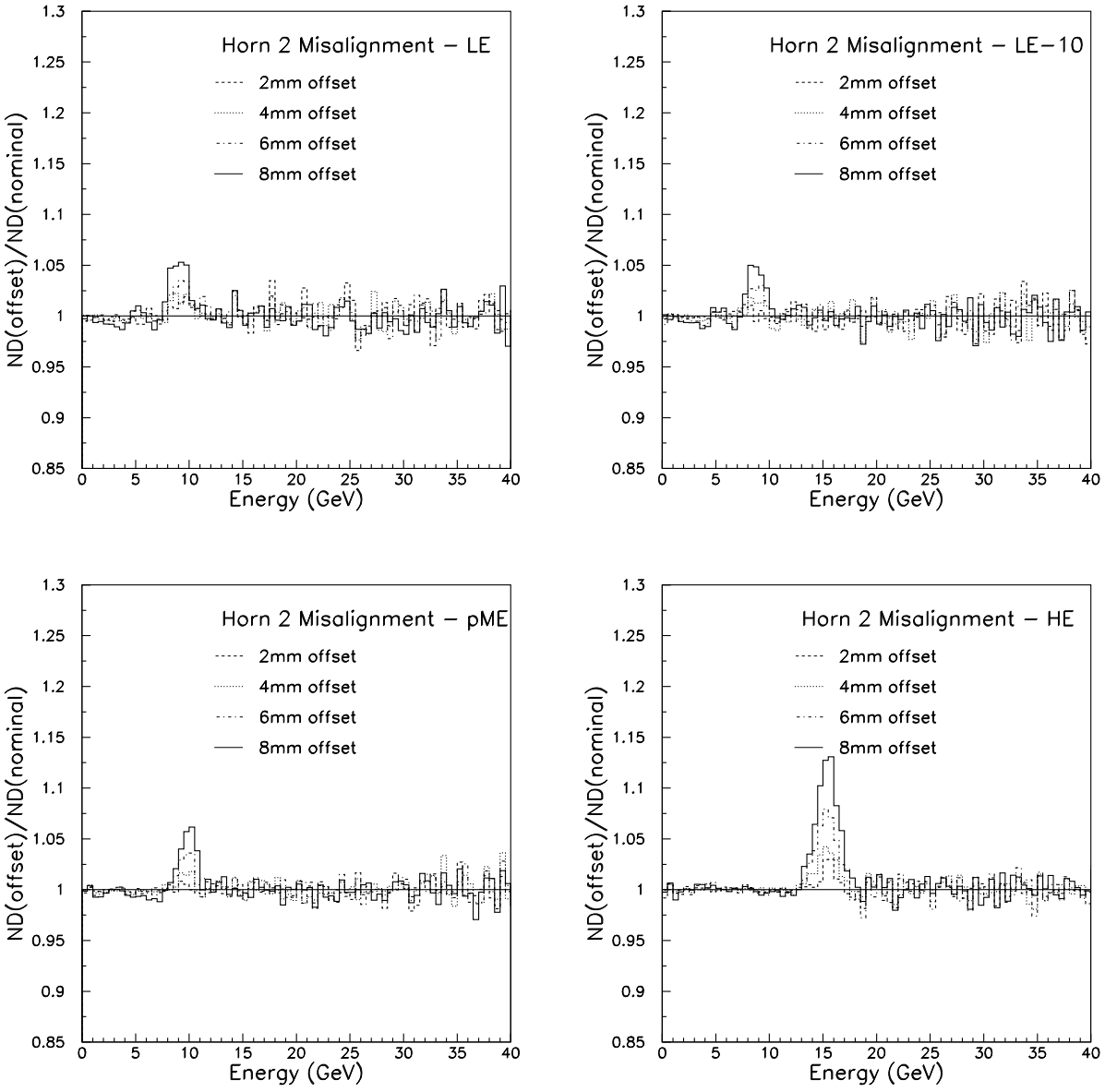

Figure 25: Near Spectrum fractional change due to Horn 2 Offset.

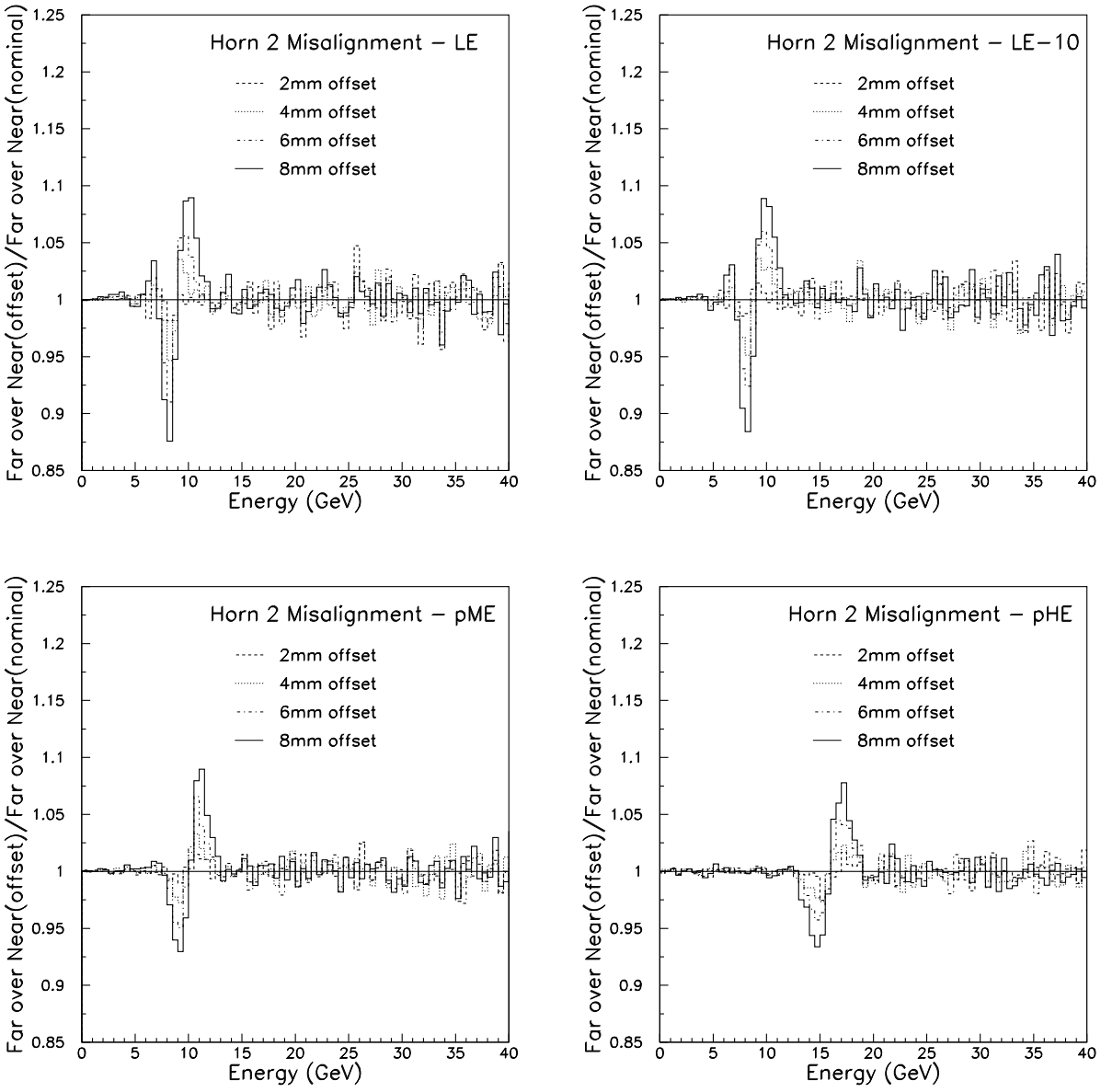

Figure 26: Far over near Ratio fractional change due to Horn 2 Offset.

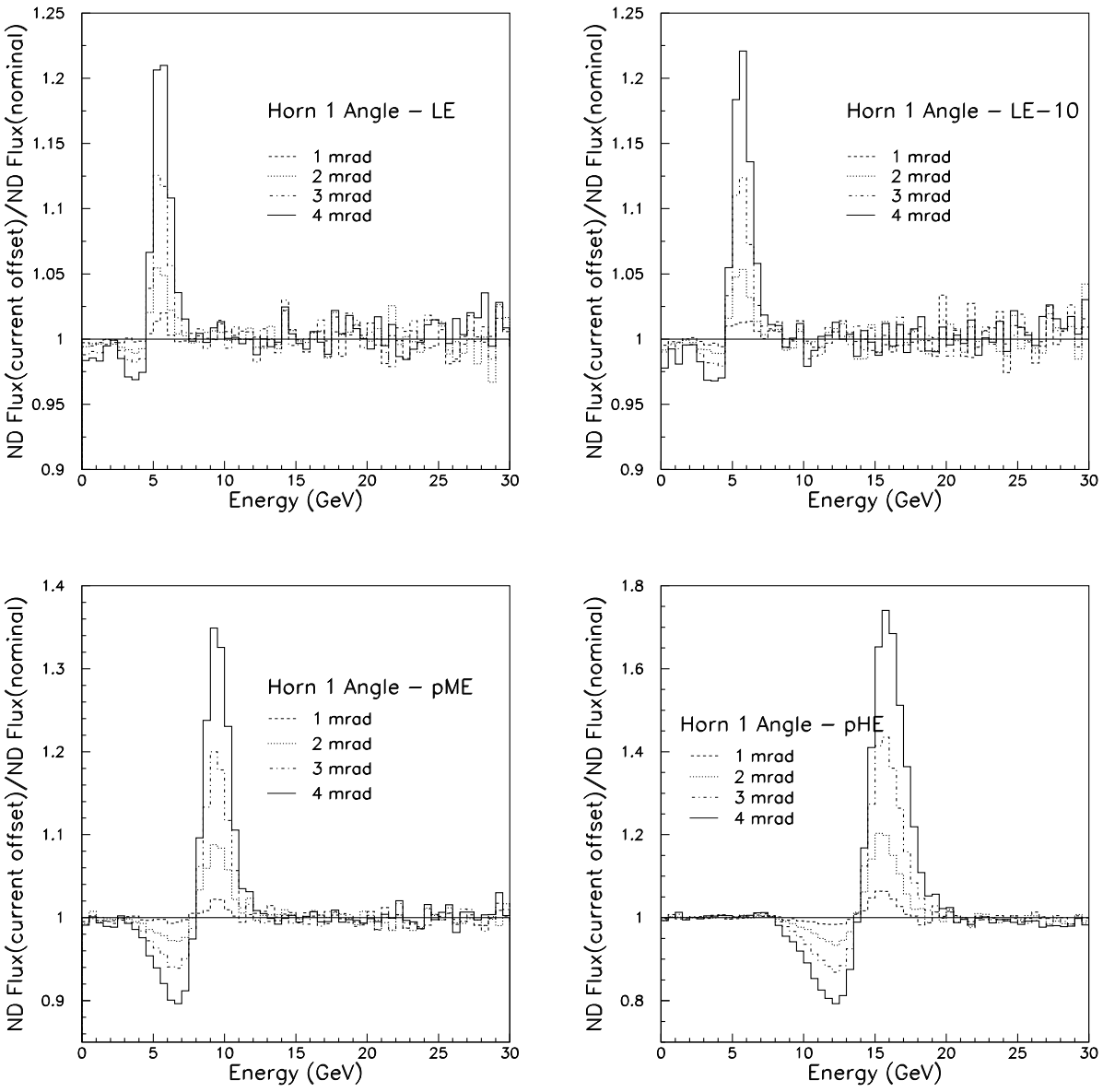

Figure 27: Near Spectrum fractional change due to Horn 1 Angle Variation.

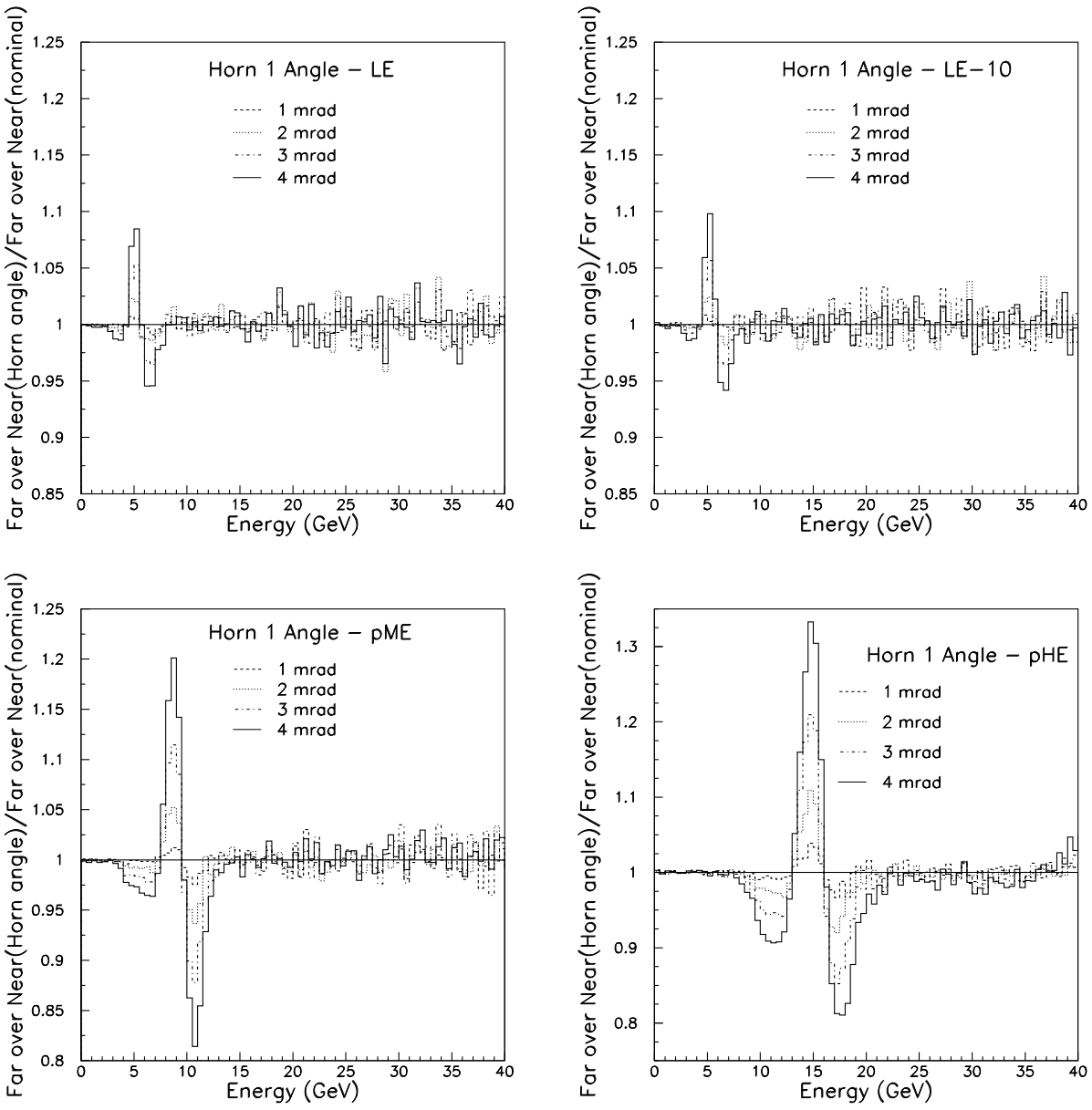

Figure 28: Far over Near Ratio fractional change due to Horn 1 Angle Variation.

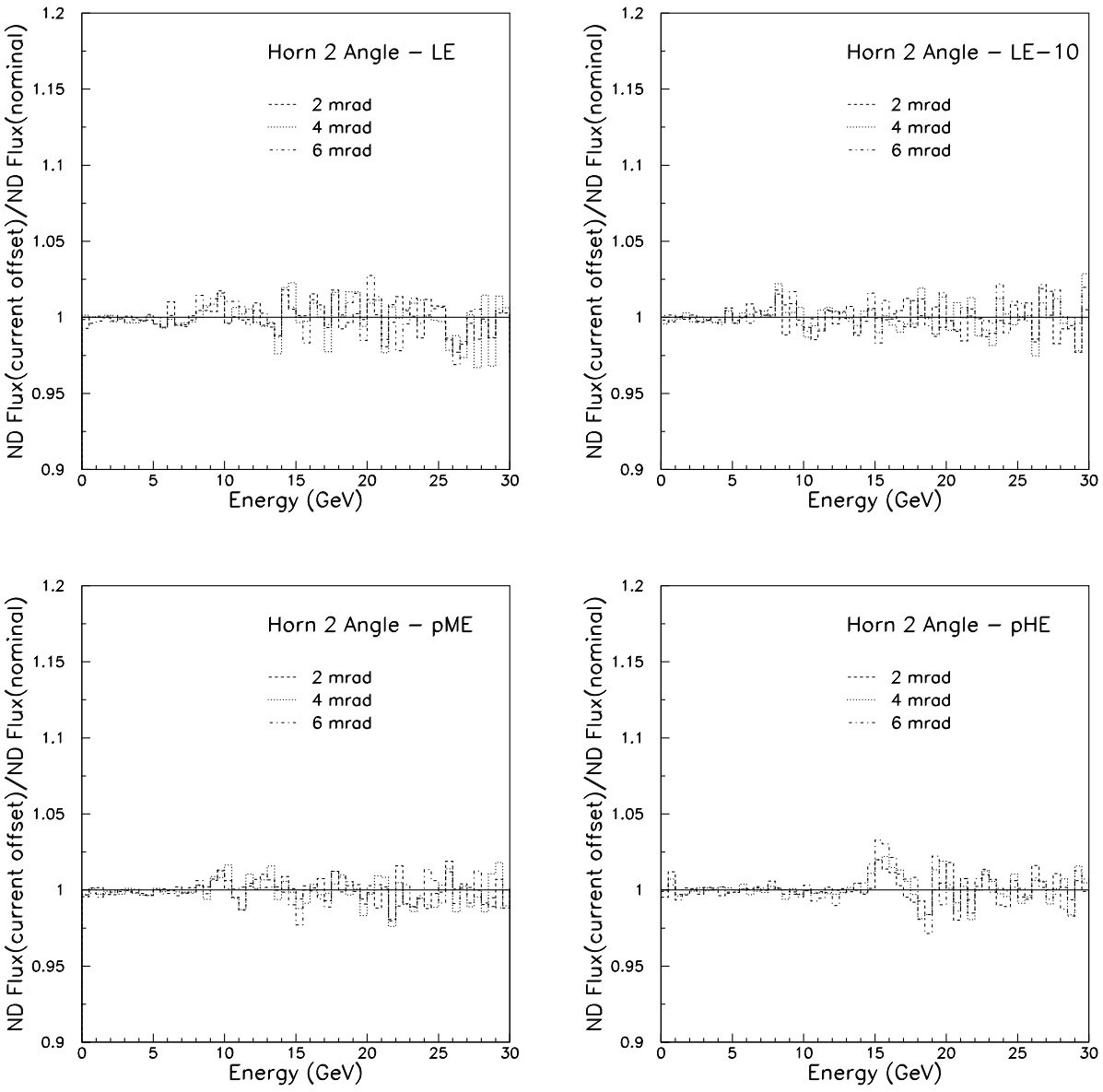

Figure 29: Near Spectrum fractional change due to Horn 2 Angle Variation.

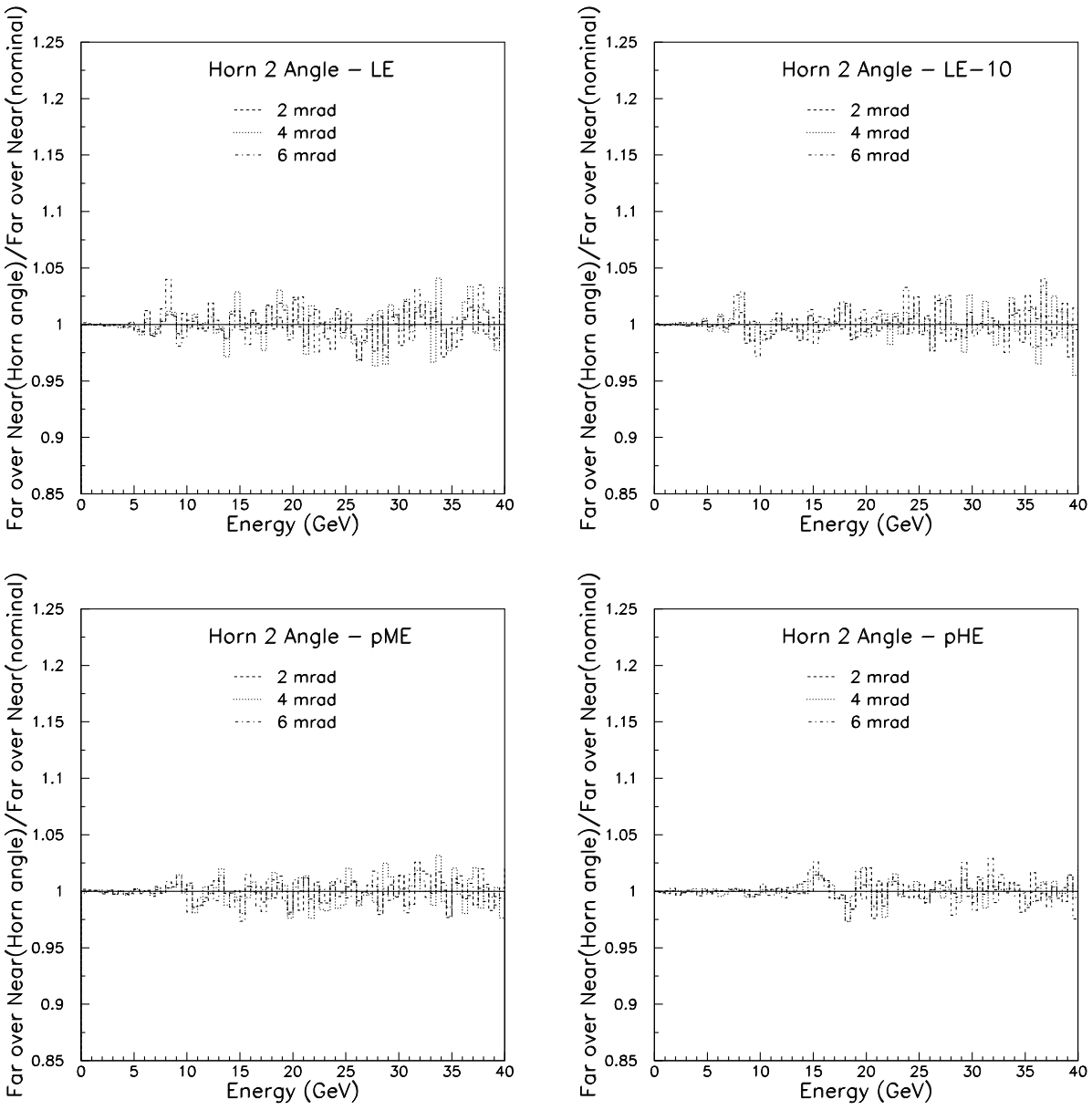

Figure 30: Far over Near Ratio fractional change due to Horn 2 Angle Variation.

5 Horn Current Uncertainties

There are two uncertainties related to the horn current. The first is the absolute value of the horn current which affects the focusing of all particles and the second comes from the uncertainty in the distribution of the curent in the horn conductors, which affects primarily a narrow portion of the neutrino spectrum. We discuss each in turn.

5.1 Horn Current Scale

The nominal horn current for the LE, pME, and pHE beams is 200 kA and the nominal current for the LE10 beam is 185 kA. These values are obtained in practice by discharging a set of capacitor banks into the horn circuit (which is largely an RL circuit). It is noticeable over the first few hours of beam operations, for example, that the horn current changes slightly (at the fraction of a percent level), gradually decreasing to an asymptotic value as the horn heats up (thermally) and the resistance increases.

A set of calibration constants for the NuMI horn current readout was recently derived in [6]. Direct measurement of the current on the horn striplines using calibrated current transformers was accomplished. Since a separate document describes this calibration procedure in detail, we may just quote the result here: it was found that the actual horn current was off by a scale factor (0.984 ± 0.005). The new version of the beam Monte Carlo (GNuMI v18) uses the 1.6% lower horn current values. Namely, 196.8kA for standard "200kA" LE, LE100 and LE250 runs and 182.1kA for "185kA" LE10 run.

To be conservative, we developed our flux uncertainties assuming the uncertainty in the knowledge of the horn current scale factor is 1%. We simulated neutrino fluxes with horn currents -2.0%, -1.0%, $+1.0\%$, and $+2.0\%$ different than the nominal value. The procedure used to find the error bar coming from horn current uncertainties was the same as the one used to find the error bars coming from alignement uncertainties of the beamline elements: different configurations (differnet horn current values and distributions) were simulated and then bin by bin fitting as described in section 4 was used to find the error band. The results are shown in Figures 31 and 32.

5.2 Skin Depth Effect

The field inside the horn is given by $B = 2I/Rc$, where I is the current enclosed in the radius R. When a particle passes through the air volume between the inner and outer horn conductors, I is clearly given by the nominally 185 kA for the LE10 beam.[1] For a particle traversing the inner conductor of the horn, however, the correct value of I to be used in modelling the horn field is a non-trivial matter. For an ideal conductor, all current would flow on the outer surface of the horn, by Gauss' Law. For a real conductor with finite conductivity, this current penetrates into the bulk of the horn conductors over a distance scale given by the skin depth, δ.

[1] Actual value is 182.1 kA, as discussed in the previous section.

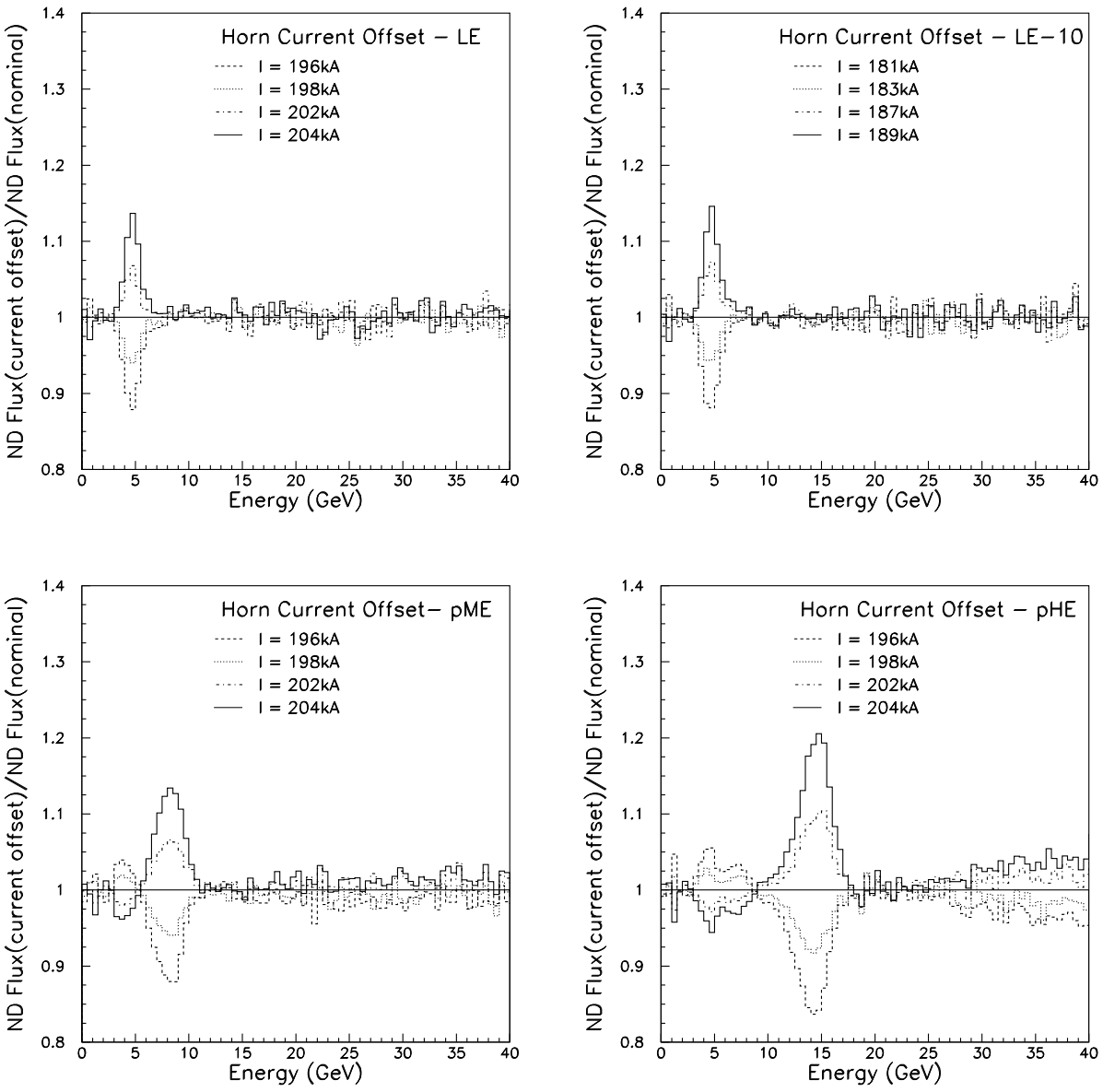

Figure 31: Near Spectrum fractional change due to Horn Current Miscalibration.

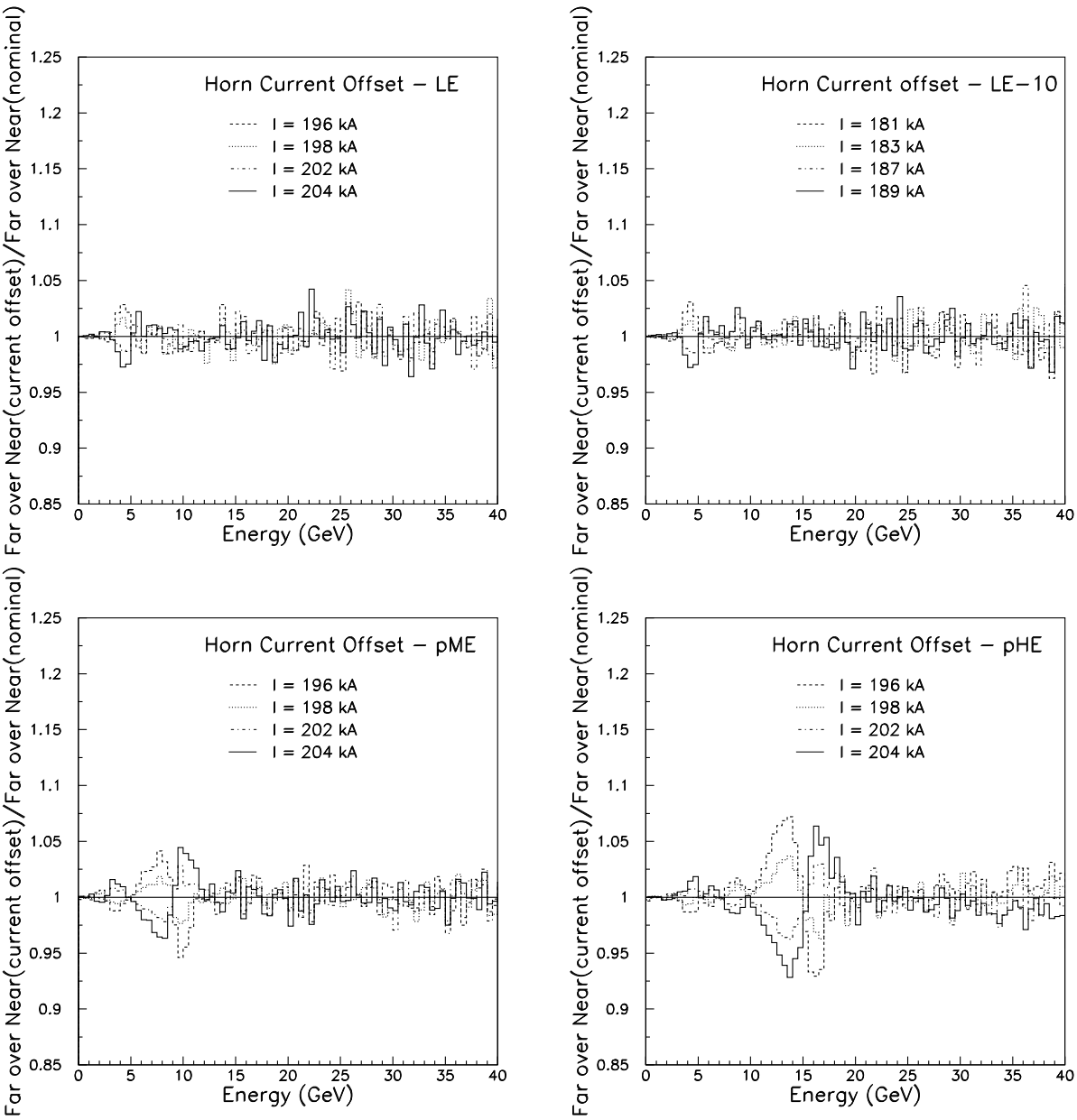

Figure 32: Far over Near Ratio fractional change due to Horn Current Miscalibration.

Thus, the concern of this section will be the proper modelling of the magnetic field of the horn in the particular volume of its inner conductor. The proper modelling of this region of the magnetic field would be expected to affect a very specific portion of the neutrino spectrum, namely that portion coming from pions which spend a great deal of time traversing the horn's inner conductor. As was noted in Section 1 and indicated schematically in Figure 1, such pions are at the smallest possible angles that receive horn focusing, and hence by virtue of the relation $p_z \approx p_T\theta$ are the pions at the upper limit of the horns' focusing. Thus, it is our expectation that this horn current modelling affects the upper edge of the focusing peaks for each beam. The uncertainty on the horn current's distribution within the inner conductor results in uncertainty in the exact magnetic field distribution in the inner conductor.

The skin depth for a conductor of semi-infinite extent is given by

$$\delta = \frac{c}{\sqrt{2\pi\sigma\mu\omega}}$$

where σ is the conductivity, μ is the permeability and ω is the frequency of the current. The frequency of relevance for the NuMI horns comes from the fact that the horn current comes in a pulse which is rougly a half sine wave with 1.0 ms rise time and 4.6 ms period. For these parameters, the skin depth is approximately 7.7mm.

The well-known exponential description of the current density penetrating a conductor's thickness is only an idealization for a conductor of semi-infinite extent. For the NuMI horns, the conductor thickness is of order 3 mm, comparable to the skin depth estimated above. Therefore the exponential is only an approximation to the real distribution. To find the current distribution we can look at the analytical solution for a current distribution in a cylindrical conductor. This solution has the following form ([7]):

$$J_z(r,t) = A[ber(\frac{\sqrt{2}}{\delta}r) - i\ bei(\frac{\sqrt{2}}{\delta}r)]e^{-i\omega t}$$

where ber and bei are "Bessel real" and "Bessel imaginary" functions, or "Kelvin" functions. The proton beam comes when the horn current is at the peak, so using the solution for the distribution we can find current density relative to surface current density at that moment:

$$|\frac{J_z(r)}{J_z(R_{out})}| = [\frac{ber^2(\frac{\sqrt{2}r}{\delta}) + bei^2(\frac{\sqrt{2}r}{\delta})}{ber^2(\frac{\sqrt{2}R_{out}}{\delta}) + bei^2(\frac{\sqrt{2}R_{out}}{\delta})}]^{1/2}$$

Using this analytical solution we find that the distribution varyies along the horn and its different at its neck then it is at its ends (Figure 33). Interestingly, this functional form deviates significantly from a simple exponential of $\delta = 7.7$ mm. Figure 33 also shows the enclosed current $I(r)$ within a radius r for each of these estimations of the horn current – the enclosed current being of course proportional to the magnetic field strength in the inner conductor.

In GNuMI, the horn current is uniformly distributed throughout the conductor and is the same along the horn. This corresponds to the case of infinite skin depth $\delta = \infty$, which

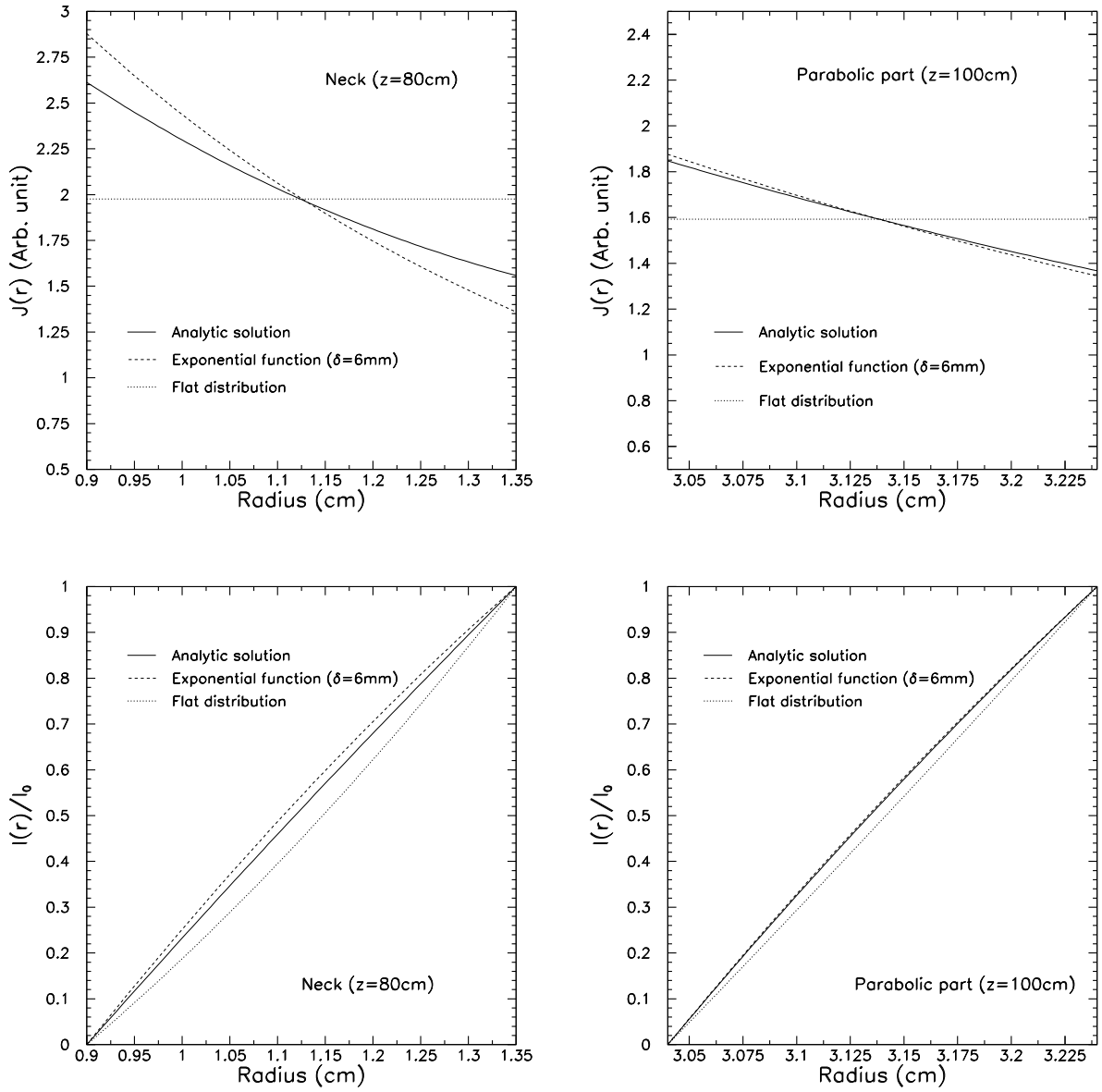

Figure 33: Comparison of three possible distributions of the horn current in the inner conductor: uniform current density (corresponding to an infinite skin depth $\delta = \infty$, an exponentially falling current distribution with $\delta = 6$ mm, and the analytical expression for a round conductor from [7]. Top plots show the current I as a function of radius r from the beam line axis. Bottom plots show the enclosed current I_{enc} inside a radius r (which is proportional to the magnetic field $B(r)$). Left plots are for the horn neck, right plots show a location along the paraboloc conductor at $z = 100$ cm.

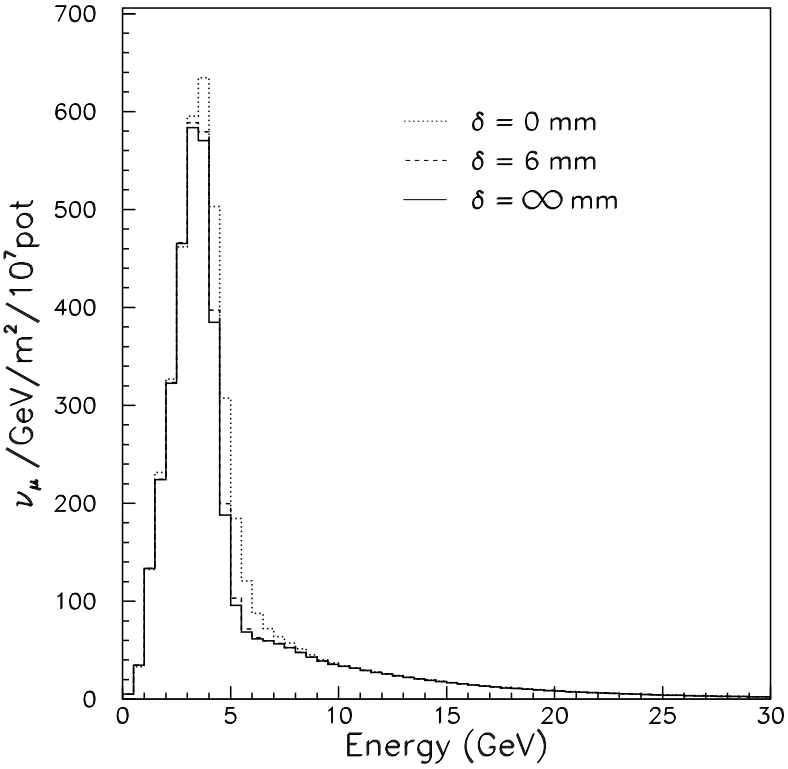

Figure 34: ν_μ flux at near detector for two extremal distributions of current in horn inner conductor. Two current distributions correspond to two different skin depths $\delta = 6mm$ and $\delta = \infty$.

is roughly true since inner horn conductor is 3mm thick and skin depth is 7.7mm as was previously noted. To estimate the error coming from this choice of modelling we ran PBEAM with different values of skin depth δ, shown for the LE10 beam in Figure 34. As might be expected, the different descriptions of the horn current mostly affect the upper edge of the focusing peak. We used the difference between $\delta = 6mm$, and $\delta = \infty$ to find the error bar. In the figure, the idealization of an ideal conductor ($\delta = 0$ mm) is also shown for reference, but is not expected to be a realistic model of our horns' current distribution.

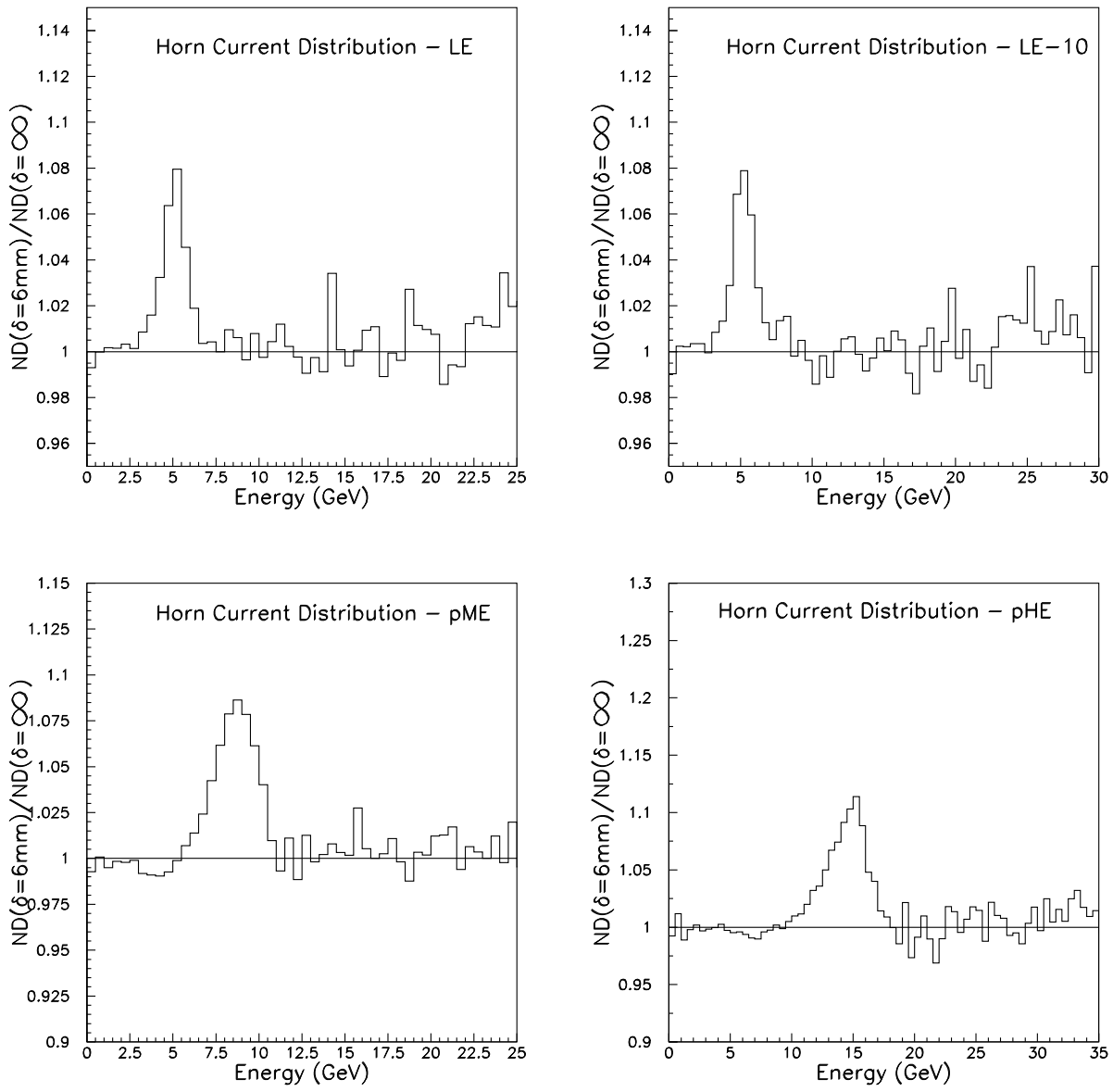

Figure 35: Near Spectrum fractional change due to Horn Current Distribution uncertainty.

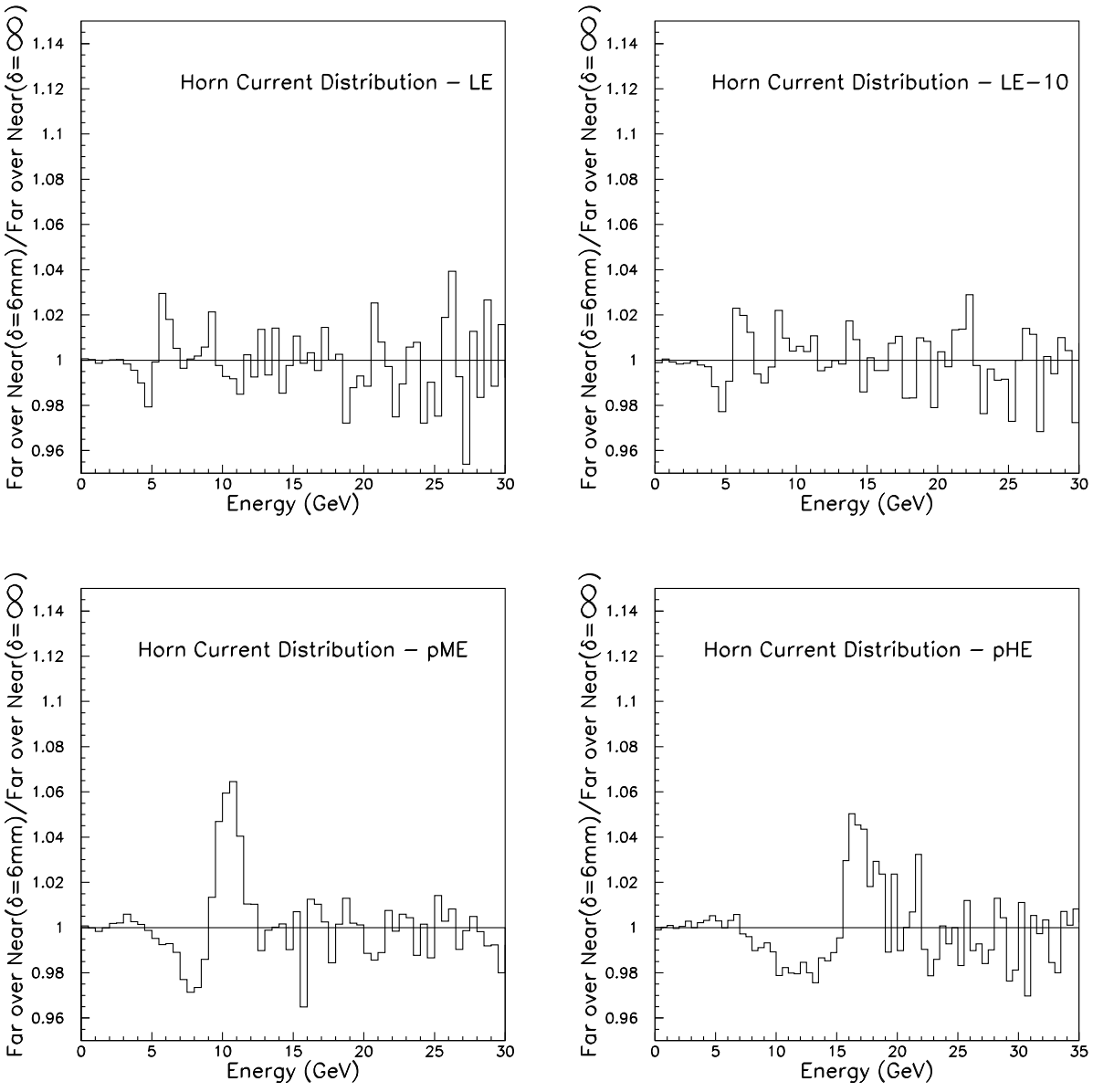

Figure 36: Far over Near Ratio fractional change due to Horn Current Distribution uncertainty.

6 Summary of Errors (Non-Hadron Production)

Before we proceed to hadron production uncertainties which, as it will be seen, mostly dominate the error band, we will summarize the uncertainties considered so far.

In the previous sections we have considered the uncertainty on number of protons hitting the target which comes from the uncertainty on proton intensity as measured by NuMI toroids and the fact that not all of the protons hit the target. Our estimate on total uncertainty coming from both effects is 2%. Misalignement of beamline elements was studied in Section 4. Misalignement of two NuMI focusing horns was studied by spliting it into the offset and the angle of the horn with respect to the primary proton axis. Misalignement of the shielding blocks inside of the chase was studied, but this didn't produce any noticable change in the flux. Flux variations due to horn current uncertainties were looked at in Section 5. The uncertainty comes from the uncertainty of the readout of absolute value of horn current and uncertainty in it's distribution inside the horn conductor. In Section 3.2 we looked at the uncertainty coming from baffle scraping since some of the protons hit the protective baffle upstream of the target.

Figures 37 and 38 show the summary of errors considered so far and Table 1 lists the uncertainties used to estimate the error bars in them.

Source	Uncertainty
POT	2.0 %
Horn offset	1.0 mm
Horn angle	0.2 mrad
Chase	1.0 cm
Horn current offset	1.0 %
Horn current distribution	$\delta = 6mm/\delta = \infty$
Baffle scraping	0.25 %

Table 1: Summary of uncertainties used to find the error bars in Figures 37 and 38.

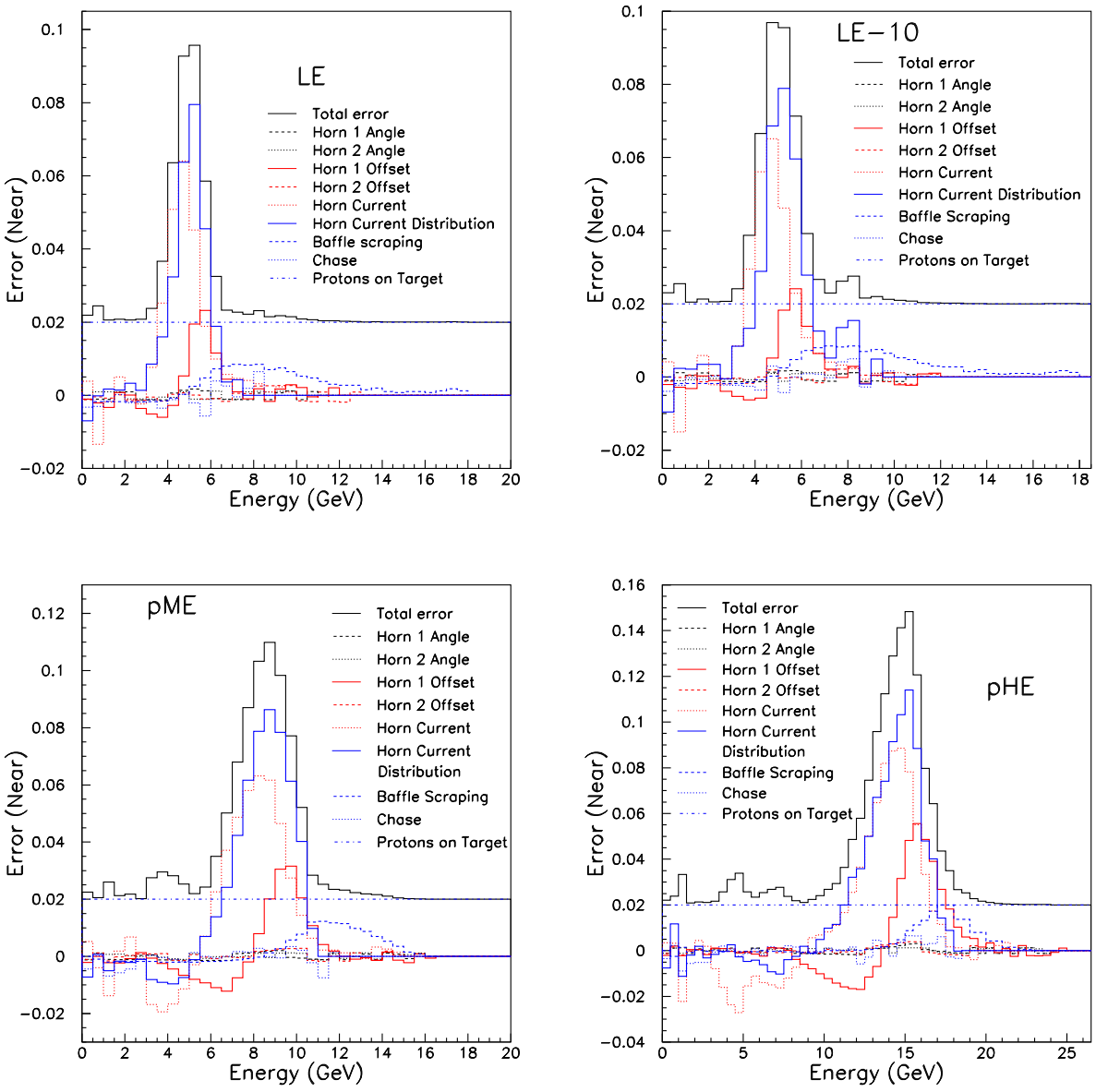

Figure 37: Near Spectrum Error.

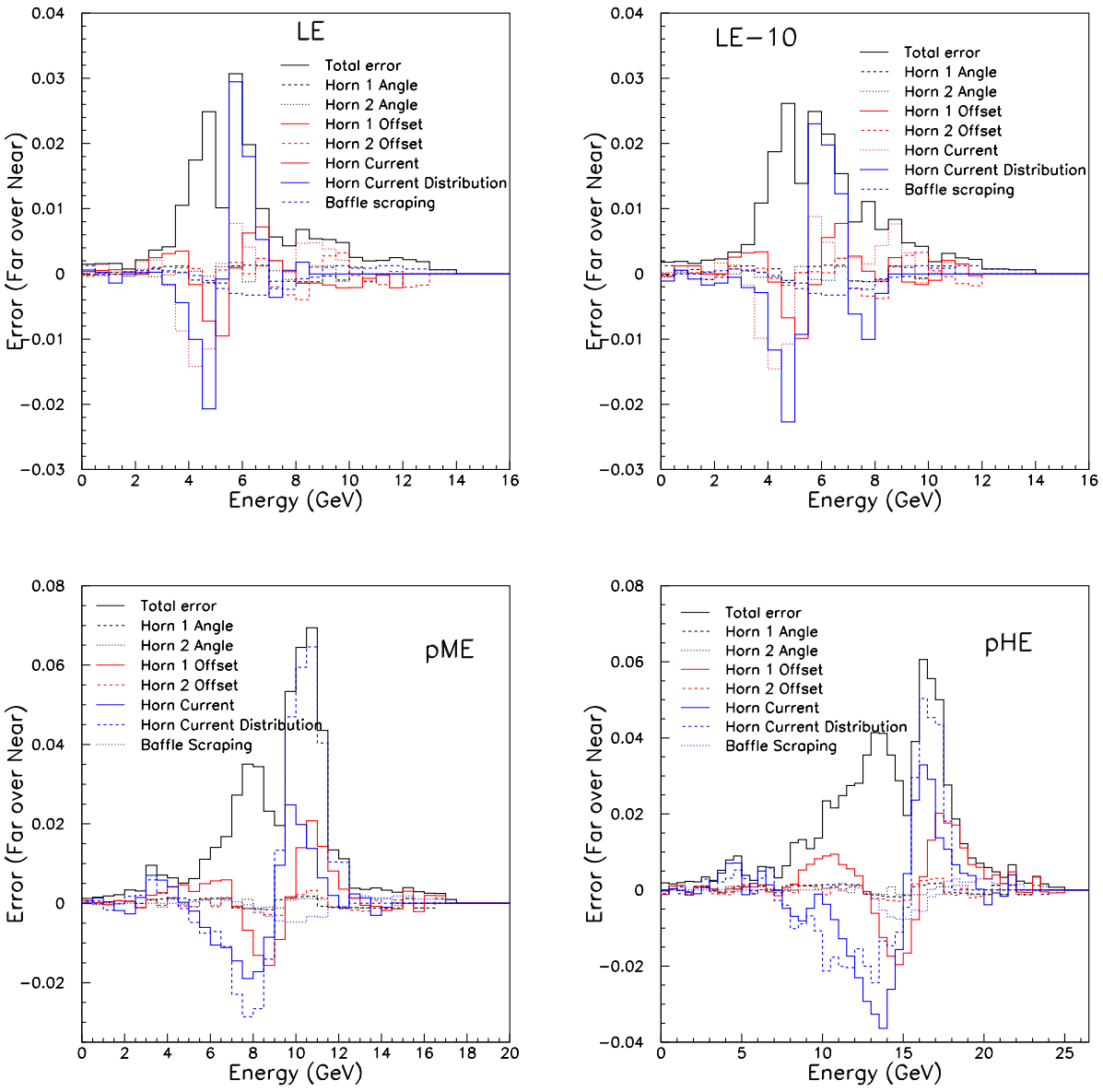

Figure 38: Far over Near Ratio Error.

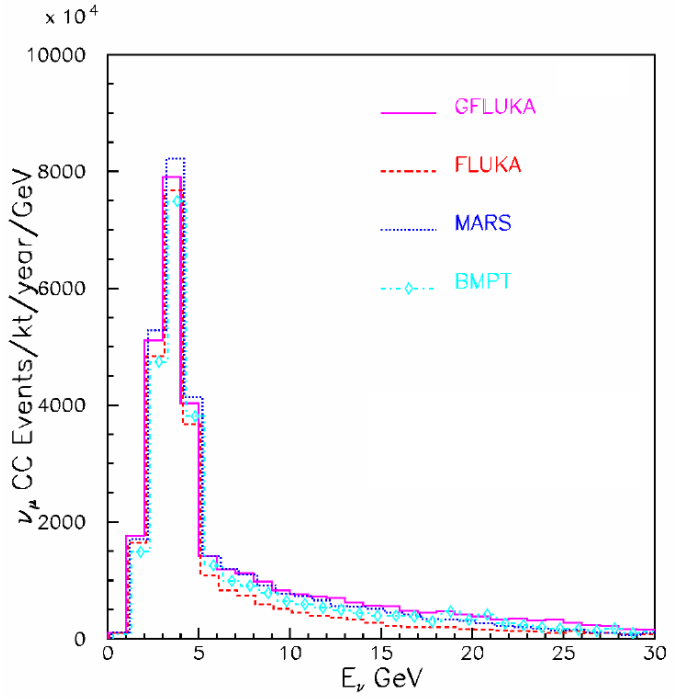

Figure 39: Hadron production model spread for LE beam at near detector.

7 Hadron Production Errors

One of the most dominant sources of systematic errors is the Hadron Production uncertainty. This has been studied in the past (see [9], and [10], and [11]). Here we summarize some of those results and include them in our total error bar. Additionally, we provide a simple cross check of the uncertainty by reweighting the target hadrons to understand the effect on the neutrino flux.

7.1 Model Spread

To estimate the hadron production uncertainty different models were considered and changes in near flux and far over near ratio were studied. The models that were considered were MARS, BMPT, Geant/Fluka, Malensek. This does not give us the true uncertainty because some of the models are correlated and some have known flaws at certain kinematic region, however it gives us a feeling for this uncertainty. Other models, such as the Malensek, Sanford-Wang, and CKP, are probably not appropriate for comparison because the are phenomenological models tuned to different energies.

Figure 39 shows CC events in Near Detector using different hadron production models. Having in mind known flaws of certain models we estimate the error on the flux at Near Detector due to Hadron Production to be approximately 8% in the focusing peak and 15% in the tail. Figure 40 shows the effect of Hadron production uncertainty on Far over Near

Ratio for three different beams (LE, pME and pHE). At high energies all 3 beams should approach same uncertainty since at high energies there is no horn focusing. Fluctuations are therefore, actually statistical fluctuations in Monte Carlo, so we apply some smoothing. We also disregard the gfluka at high energies since its known that it exaggerates the particle flux at high x_F.

It is worth commenting that the high energy tail is the most uncertain portion of the neutrino spectrum in any of the beam configurations, both from the point of view of the raw spectrum, but also for the F/N ratio. This is because the high energy portion of the spectrum consists of unfocused parent pions and kaons which pass throught the field-free necks of the focusing horns. Receiving no focusing, they diverge with a maximum angle of ~ 0.1 mr, defined by the horn neck apertures. The energy of the neutrinos from these parents is thus quite sensitive to the divergence of the parent particles off the target, or in other words to the differential cross section $d^2\sigma/dpd\Omega$ or $d^2\sigma/dpdp_T$ for pions and kaons off the target. The horns, which attempt to focus all pion rays from point-to-parallel, reduce this divergence and thus reduce the sensitivity of the spectrum to those particles' creation spectra.

It is also worth noting that the hadron production uncertainty, while over-estimated by virtue of our including some less credible models such as Geant/Fluka, is also potentially underestimated due to correllations between the models. In particular, the high energy tail, which has a strong contribution from kaon decays, could have an additional uncertainty because the kaon description in Fluka and MARS appears to be quite similar.

More recently, GNuMI v.18 fluxes were made available to the collaboration which updated the work of NuMI-B-768. Alysia Marino, Francisco Yumiceva, Hyejoo Kang, and Tingjun Yang improved the target geometry models and used these models to create a 'list' of pions and kaons off the target as predicted by the newer FLUKA-2005 and MARS-v.15 monte carlos. Although the fluxes did change as compared to the older FLUKA-2001 and MARS-v.14 utilized in NuMI-B-768, a similar spread of models was observed in the more recent work. Documentation of the GNuMI-v.18 fluxes is available at the Beam Monte Caro web site: `http://www.hep.utexas.edu/numi/beamMC/`.

7.2 Particle Reweighting

Table 2 shows the mean transverse momentum of pions created in a graphite target by a proton beam of 120 GeV. The table compares the $\langle p_T \rangle$ from several models of hadron production, including some which are "disfavored" by current particle production data (though we have not specifically endeavored to understand the level of consistency or inconsistency). Because the NuMI horns focus particles most efficiently at $p_T \sim 250$ MeV/c, the spread in the models shown results in a varying yield of neutrinos if these various models are used as inputs to the beam MC: models predicting a narrow p_T spectrum would be expected to translate to a greater neutrino flux per proton on target.

We attempted to cross check our hadron production uncertainty by simply reweighting the target pions and kaons to give stiffer or softer p_T spectra. Figure 41 shows the pion transverse

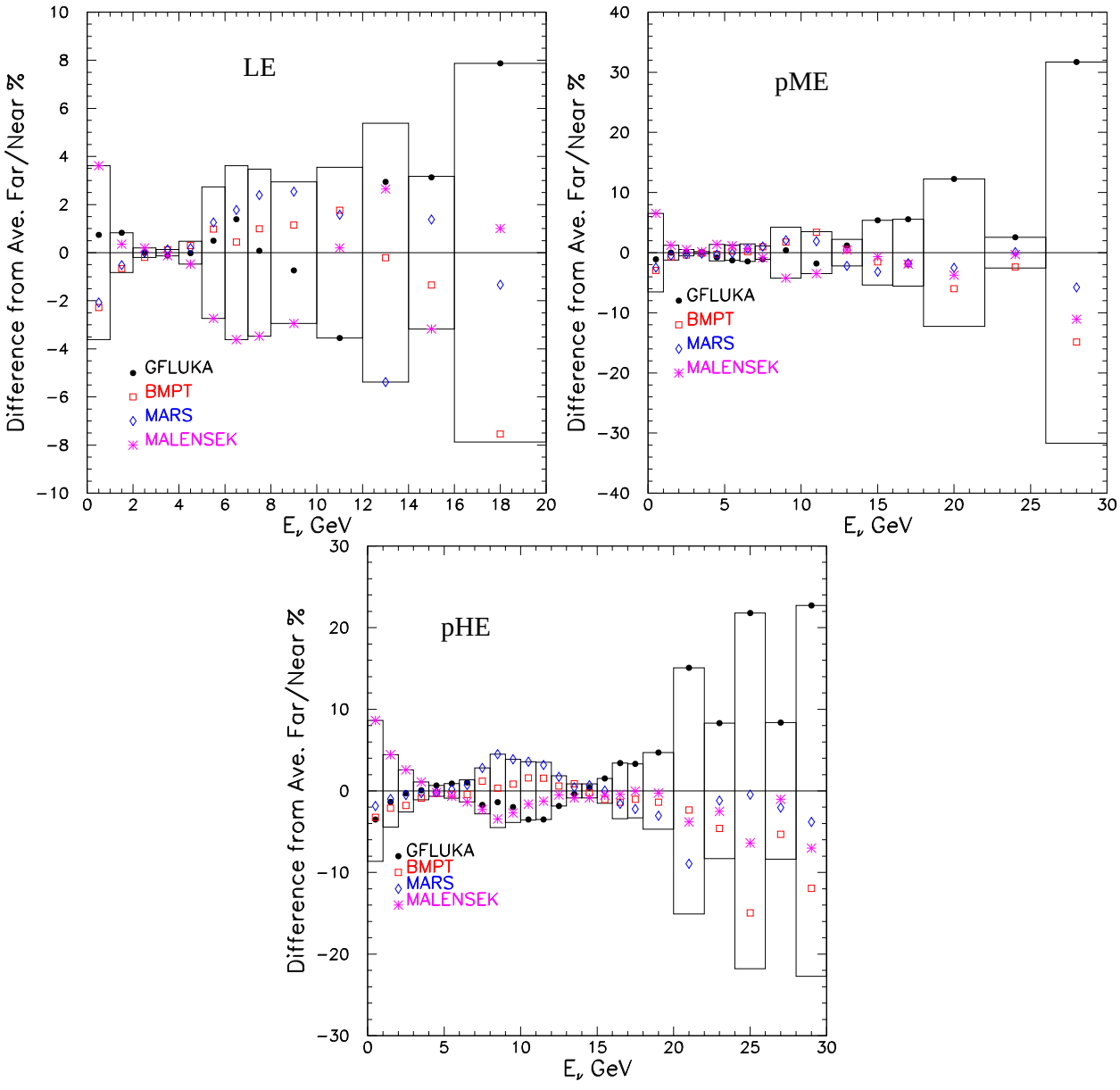

Figure 40: Hadron production model spread for Far over Near ratio.

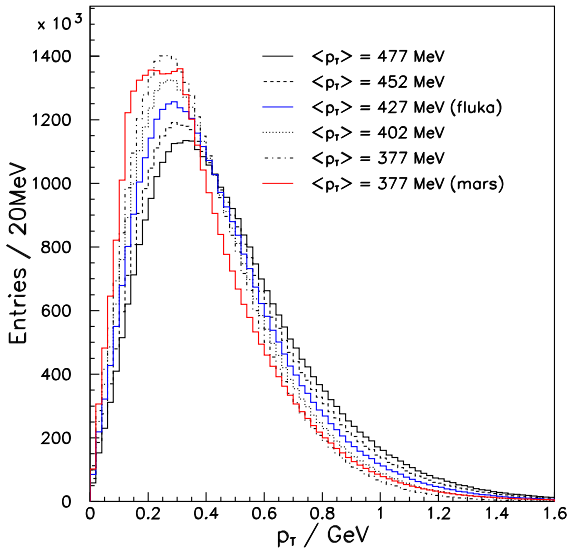

Figure 41: Transverse momentum of pions created in a graphite target by a proton beam of 120 GeV, as predicted by the FLUKA-2005 and MARS-v.15 Monte Carlos. Also shown are several versions of the FLUKA distribution skewed to shift $\langle p_T \rangle$.

momentum distributions taken from the two Monte Carlos, MARS-v.15 and FLUKA-2005, used in GNuMI-v.18. As is indicated in the table, MARS predicts a softer p_T spectrum (which translates to a higher neutrino flux), with $\langle p_T \rangle = 380$ MeV/c, as compared to FLUKA which has $\langle p_T \rangle = 430$ MeV/c. We therefore skewed the FLUKA p_T distribution so as to give shifts in $\langle p_T \rangle$ comparable to the difference between MARS and FLUKA. As can be seen in the Figure, the skewed FLUKA distribution is similar to the MARS p_T distribution.

Figure 42 shows the transverse momenta of pions which result in neutrinos in the ND. That is, it is the same distribution as Figure 41, but with an extra neutrino weighting applied

Model	$\langle p_T \rangle$ (GeV/c)
Geant/Fluka	0.37
Fluka 2005	0.43
Sanford-Wang	0.42
CKP	0.44
Malensek	0.50
MARS-v.15	0.38

Table 2: Comparison of mean transverse momenta of particles from a thick graphite target struck by 120 GeV protons.

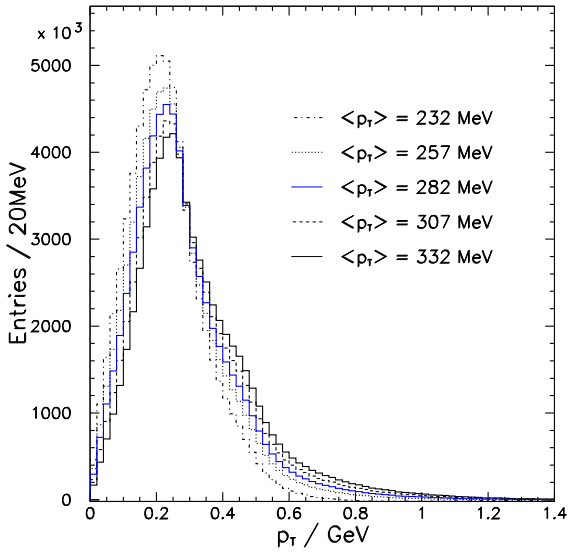

Figure 42: Transverse momenta of particles from the target as predicted by FLUKA-2005, but for only those particles which produce a CC neutrino interaction in the ND (*cf.* Figure 41).

from the beam MC. As expected, the mean p_T is shifted downward, reflecting the selection by the focusing horns. We again show the spectrum distorted by ± 25 MeV and ± 50 MeV. Because the horn focusing reduces $\langle p_T \rangle$ by almost half, we will take the maximum allowable p_T shifts to be ± 25 MeV,

Figures 43 and 44 show what happens to the ND CC spectrum when $\langle p_T \rangle$ is shifted as in Figure 42. As can be seen, a shift of $\langle p_T \rangle$ by 25 MeV changes the neutrino flux in the focusing peak changes by $\sim 5-10\%$, while in the high energy tail it changes by 15-20%. This is consistent with the estimated flux error from hadron production estimated by the spread of various models. It is of interest to note that skewing the p_T distribution in the pME and particularly the pHE beams seems to have the effect of making a softer or harder neutrino spectrum. The sign of the effect is that a broadened p_T spectrum with $\langle p_T \rangle = 332$ MeV shows a softer neutrino spectrum. This is reasonable, since the pions with broadened p_T enter the decay volume with larger angles, so the decay angles of neutrinos hitting the ND must be larger, and this reduces the neutrino energy.

Figures 45 and 46 show the effect of this same p_T skewing on the F/N ratio. Similar to the systematic error derived from the spread of models, this skewing of the parent particles would seem to suggest that the F/N ratio is stable at the 5% level in the focusing peak for the worst-case of the pHE beam, and is better than 3% in the LE beam. The spread F/N in the high energy tail is a about 5%, which again is consistent with the model spread estimate and the hadron production uncertainties recommended in Table 3.

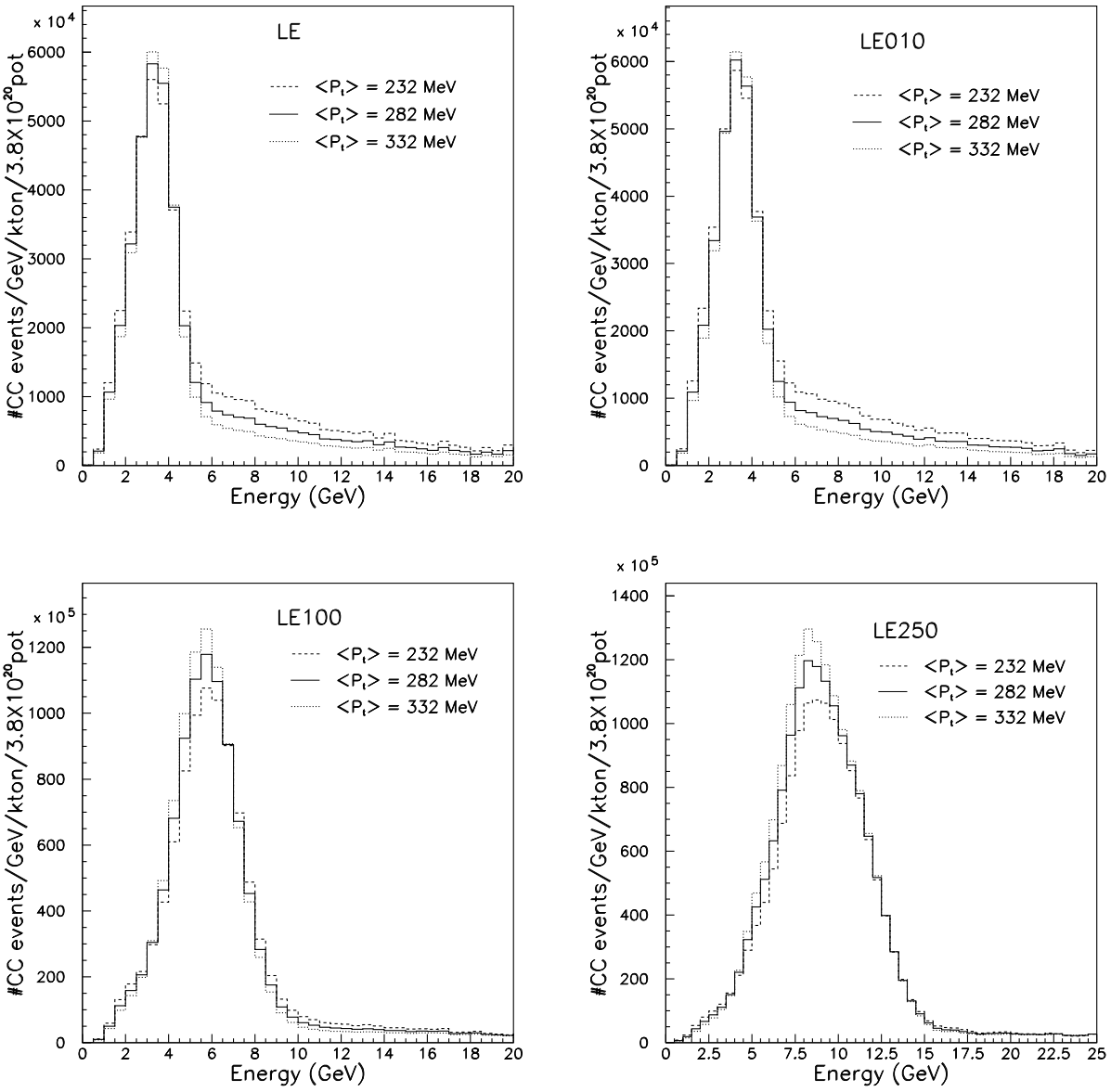

Figure 43: Neutrino spectra in the ND as predicted from GNuMI-v.18 (FLUKA-2005) in the LE (top left), LE10 (top right), pME (bottom left), and pHE (bottom right). In each plot, the nominal pion $\langle p_T \rangle$ of 282 MeV/c has been skewed by $\pm$50 MeV/c.

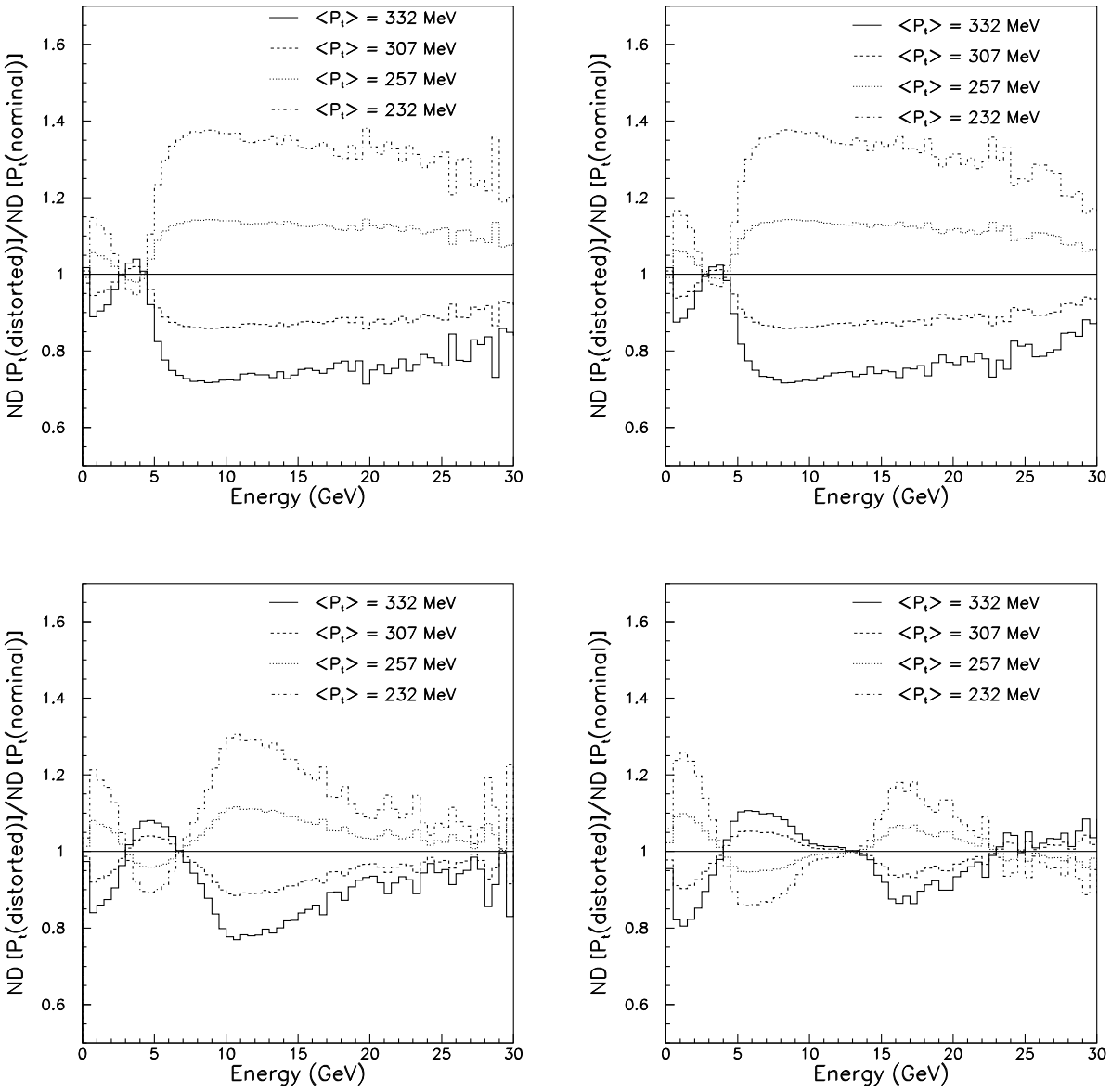

Figure 44: Ratio of neutrino spectra in the ND as predicted from the skewed p_T spectra of Figure 43 to the nominal spectra generated with $\langle p_T \rangle = 282$ MeV/c.

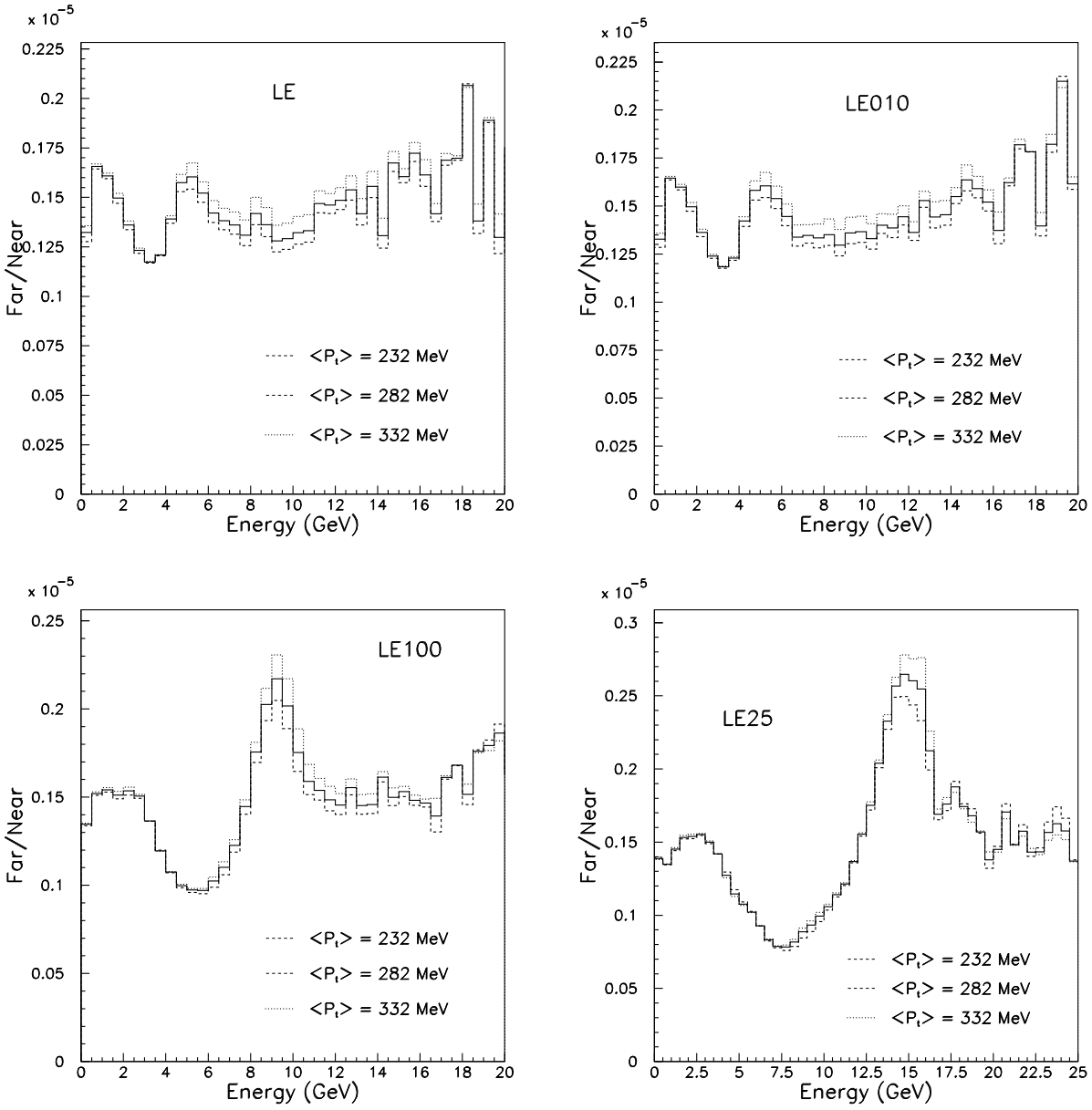

Figure 45: F/N ratio as predicted from GNuMI-v.18 (FLUKA-2005) in the LE (top left), LE10 (top right), pME (bottom left), and pHE (bottom right). In each plot, the nominal pion $\langle p_T \rangle$ of 282 MeV/c has been skewed by $\pm$50 MeV/c.

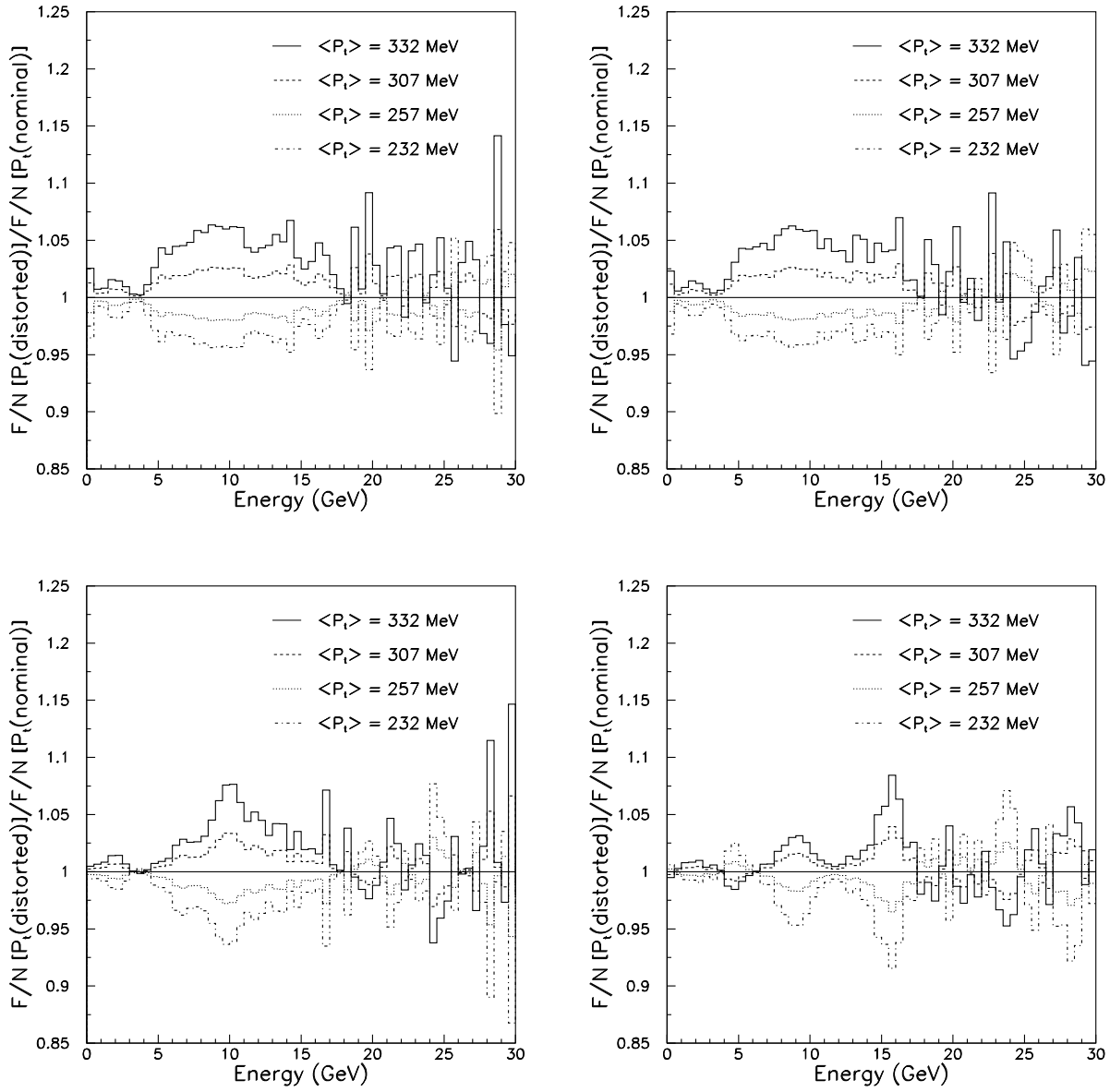

Figure 46: Double-ratio of F/N ratio as predicted from the skewed p_T spectra of Figure 45 to the nominal spectra generated with $\langle p_T \rangle = 282$ MeV/c.

	Near			Far over Near		
E_ν	LE	ME	HE	LE	ME	HE
0.00	0.08	0.08	0.08	0.036	0.05	0.085
0.50	0.08	0.08	0.08	0.036	0.05	0.085
1.00	0.08	0.08	0.08	0.018	0.015	0.041
1.50	0.08	0.08	0.08	0.018	0.015	0.041
2.00	0.08	0.08	0.08	0.003	0.01	0.025
2.50	0.08	0.08	0.08	0.003	0.01	0.025
3.00	0.08	0.08	0.08	0.003	0.005	0.012
3.50	0.08	0.08	0.08	0.003	0.005	0.012
4.00	0.08	0.08	0.08	0.005	0.018	0.007
4.50	0.08	0.08	0.08	0.005	0.018	0.007
5.00	0.15	0.08	0.08	0.027	0.018	0.01
5.50	0.15	0.08	0.08	0.027	0.018	0.01
6.00	0.15	0.08	0.08	0.04	0.019	0.016
6.50	0.15	0.08	0.08	0.04	0.019	0.016
7.00	0.15	0.08	0.08	0.036	0.015	0.027
7.50	0.15	0.08	0.08	0.036	0.015	0.027
8.00	0.15	0.08	0.08	0.033	0.04	0.043
8.50	0.15	0.08	0.08	0.033	0.04	0.043
9.00	0.15	0.15	0.08	0.033	0.04	0.04
9.50	0.15	0.15	0.08	0.033	0.04	0.04
10.00	0.15	0.15	0.08	0.035	0.035	0.036
10.50	0.15	0.15	0.08	0.035	0.035	0.036
11.00	0.15	0.15	0.08	0.035	0.035	0.033
11.50	0.15	0.15	0.08	0.035	0.035	0.033
12.00	0.15	0.15	0.08	0.052	0.02	0.017
12.50	0.15	0.15	0.08	0.052	0.02	0.017
13.00	0.15	0.15	0.08	0.052	0.02	0.01
13.50	0.15	0.15	0.08	0.052	0.02	0.01
14.00	0.15	0.15	0.08	0.055	0.05	0.012
14.50	0.15	0.15	0.08	0.055	0.05	0.012
15.00	0.15	0.15	0.08	0.055	0.05	0.017
15.50	0.15	0.15	0.15	0.055	0.05	0.017
16.00	0.15	0.15	0.15	0.058	0.05	0.03
16.50	0.15	0.15	0.15	0.058	0.05	0.03
17.00	0.15	0.15	0.15	0.058	0.05	0.03
17.50	0.15	0.15	0.15	0.058	0.05	0.03
18.00	0.15	0.15	0.15	0.058	0.055	0.055
18.50	0.15	0.15	0.15	0.058	0.055	0.055
19.00	0.15	0.15	0.15	0.058	0.055	0.055
19.50	0.15	0.15	0.15	0.058	0.055	0.055
20.00	0.15	0.15	0.15	0.058	0.058	0.058

Table 3: Final recommendations for hadron production errors.

8 Final Error Bar

Figures 47 and 48 show the total error on neutrino flux and far over near ratio that we get when we sum in quadrature errors from sections 2-7.

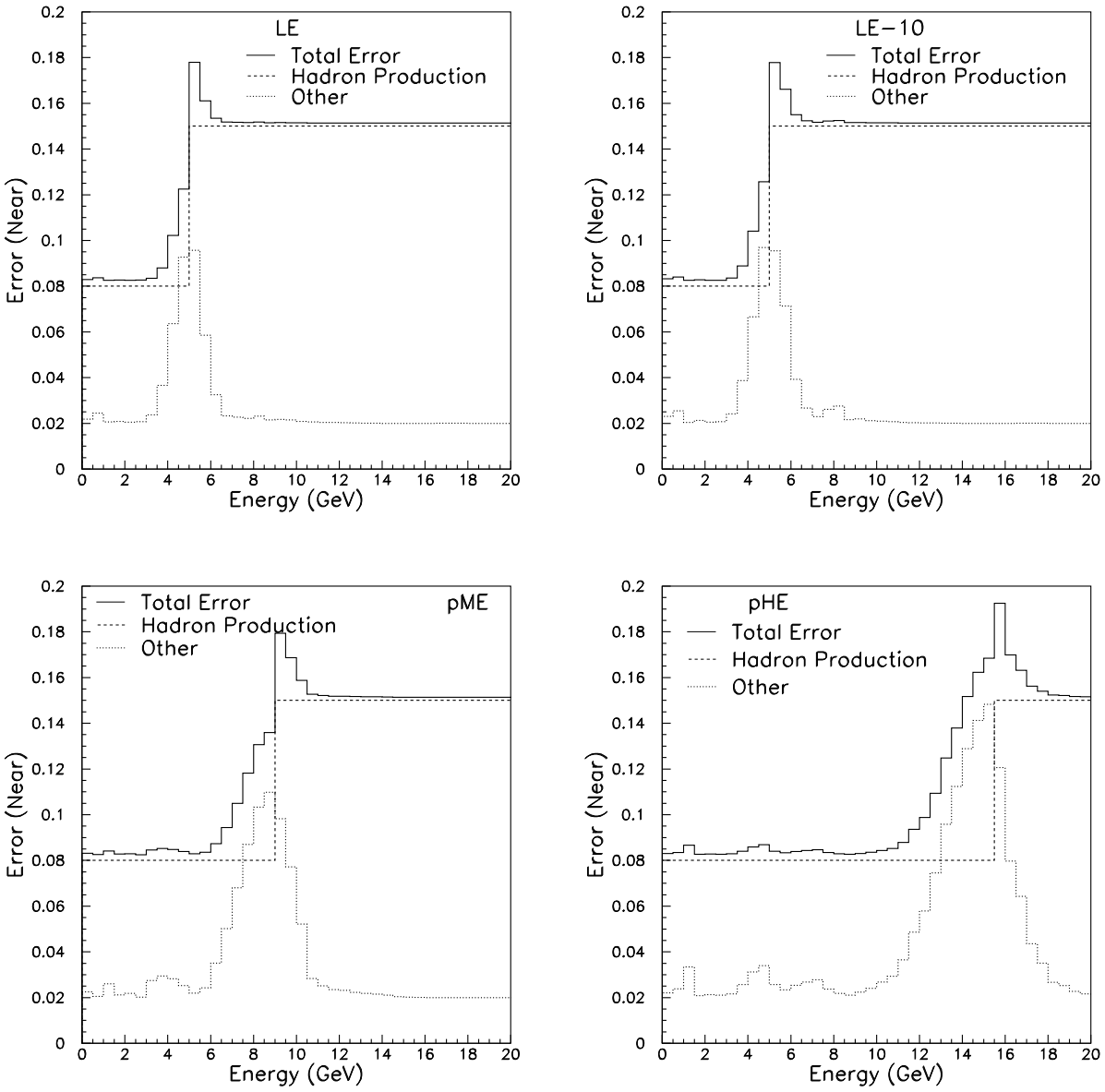

Figure 47: Final error bar for ν_μ flux at Near Detector. Other represents errors coming from uncertainties considerd in sections **??**-3.2.

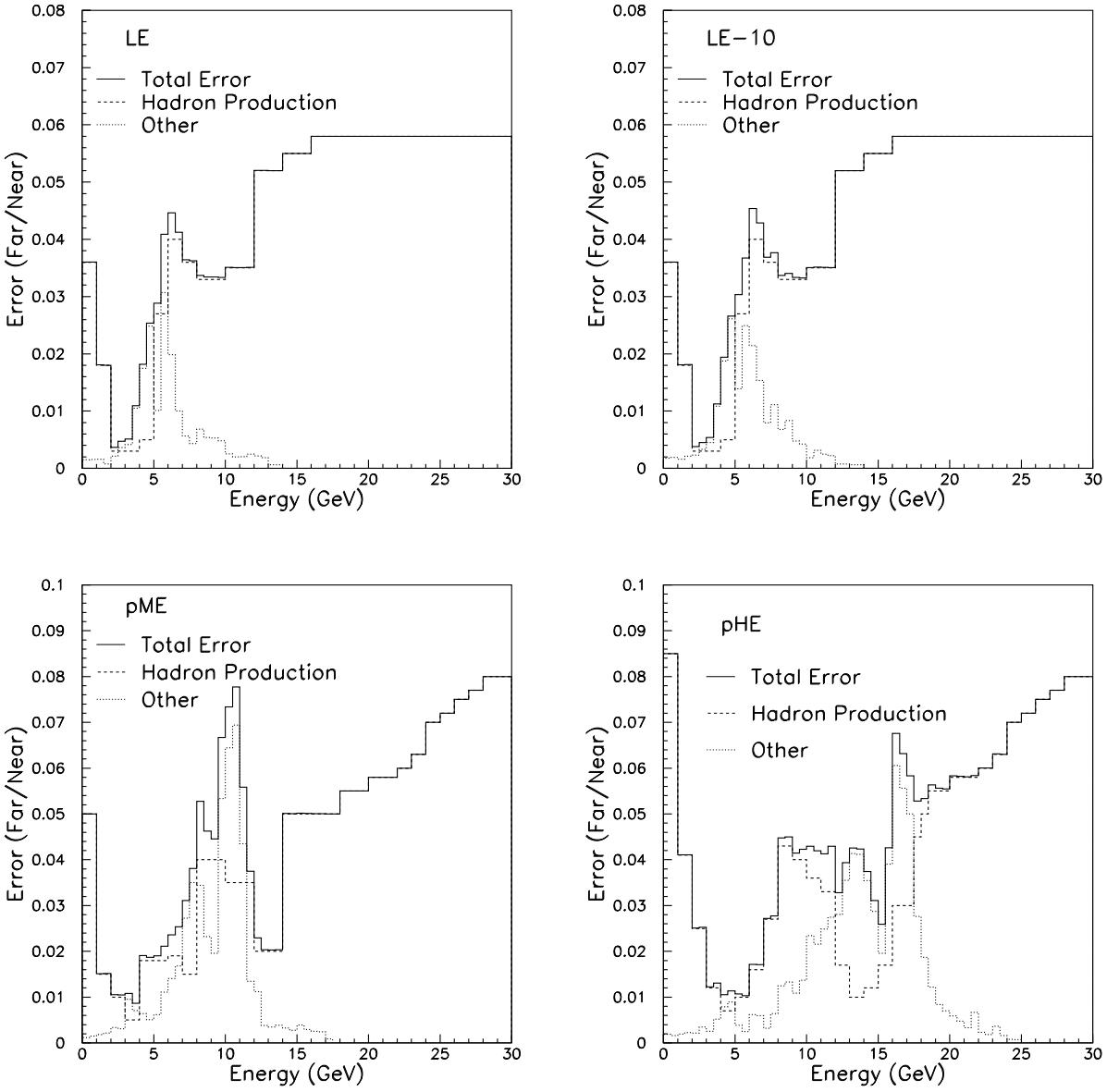

Figure 48: Final error bar on Far over Near ratio for ν_μ's. Other represents errors coming from uncertainties considerd in sections **??**-3.2.

9 Neutrino Spectrum

Finally we can apply all of the errors to the neutrino flux as we get it from gnumi. Figure 49 shows the errors applied to the Near Detector CC events spectra and Figure 50 shows the errors applied to far over near ratio.

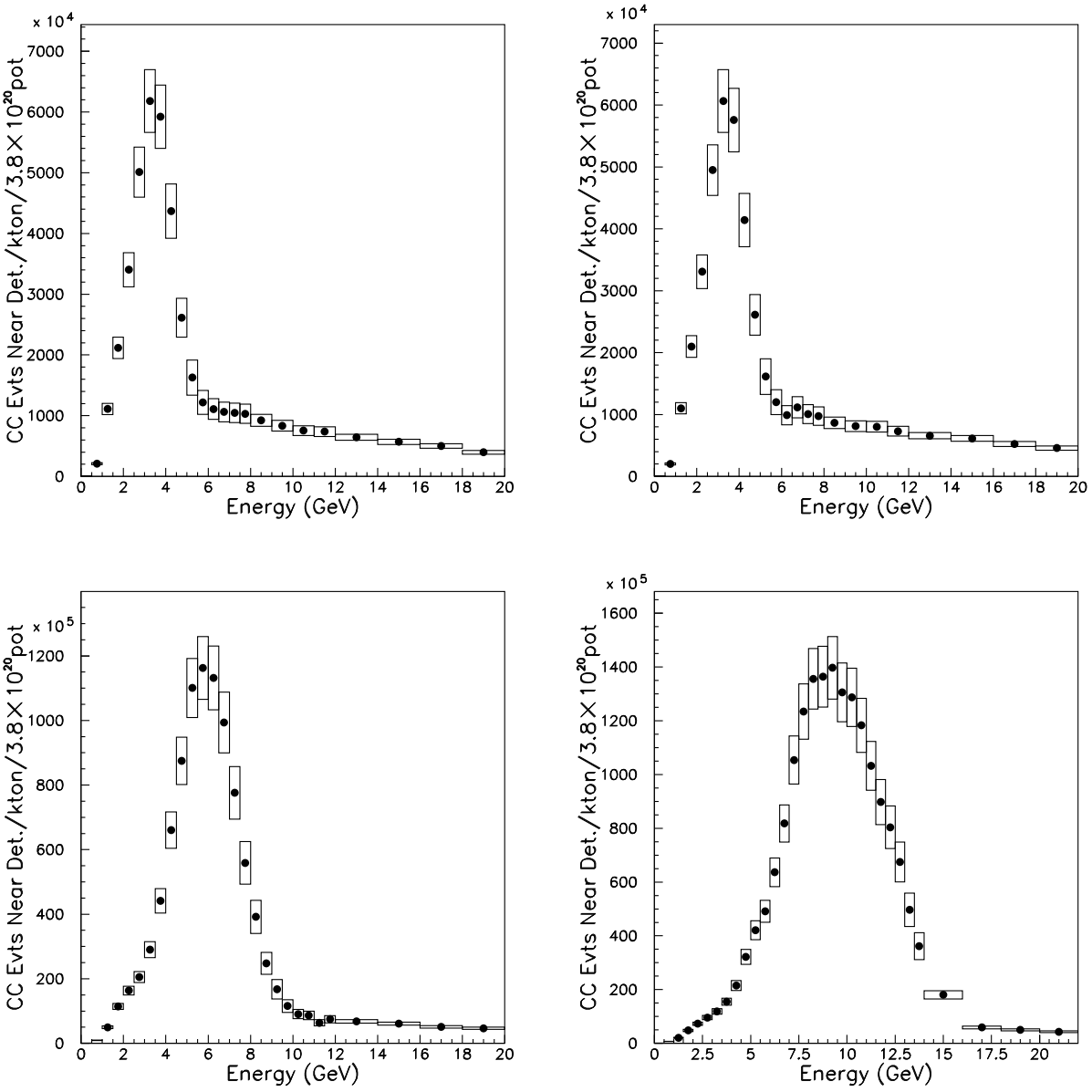

Figure 49: Near Spectrum Error.

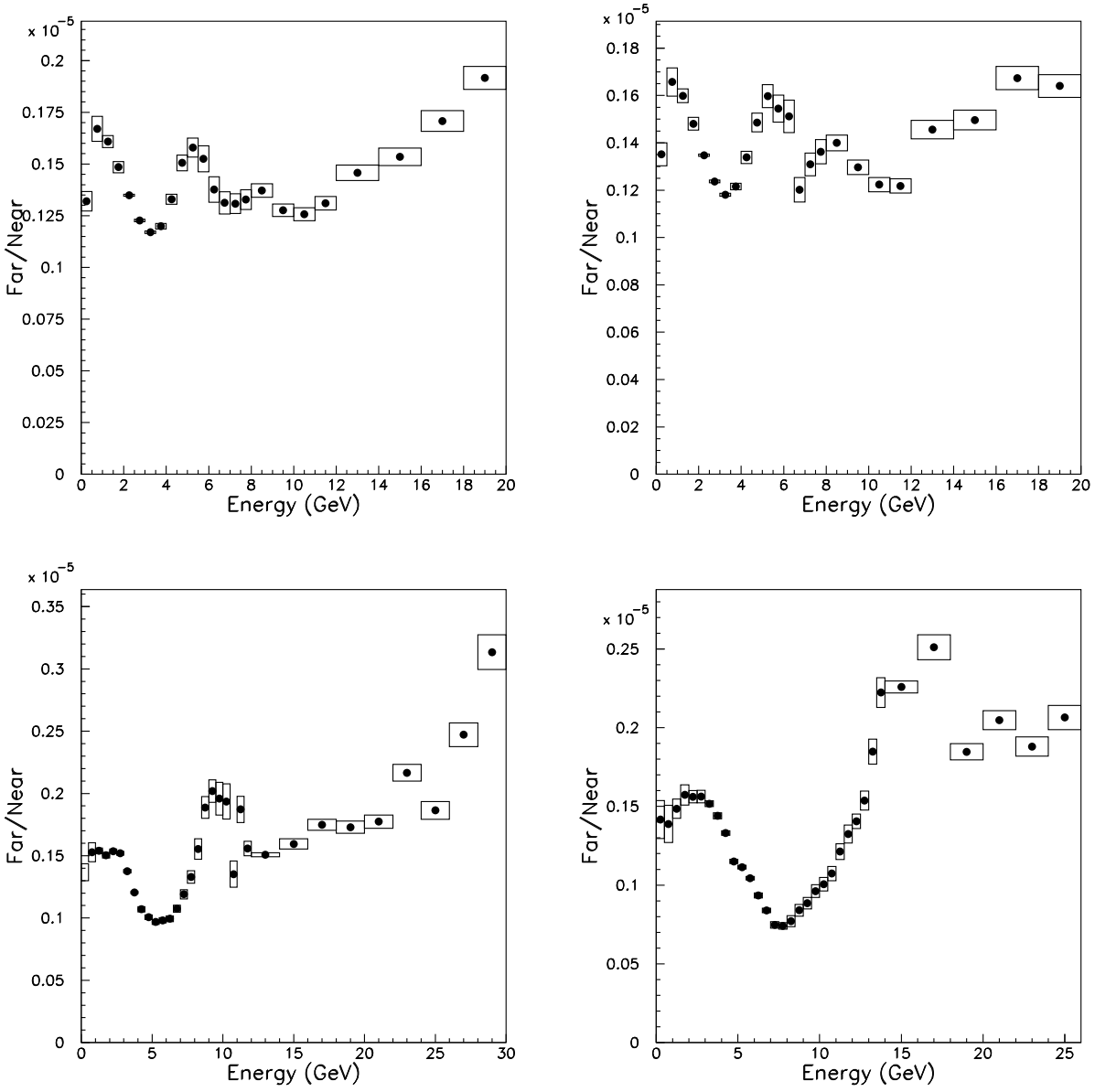

Figure 50: Far over Near Ratio Error.

References

[1] M. Bishai, A.D. Marino, B. Viren, "Protons on Target Counting", forthcoming minos-doc.

[2] D. Jensen, MINOS-doc-1229-v1, "Toroid Uncertainty", presented at October, 2005, MINOS Collaboration meeting.

[3] S. Kopp *et al*, "Segmented Foil SEM Grids at Fermilab," Fermilab-Conf-05-XXX, submitted to 2005 IEEE Nuclear Science Symposium, Puerto Rico.

[4] R. Zwaska, PhD Thesis, University of Texas at Austin, December, 2005.

[5] M. Kostin, S. Kopp, M. Messier, D. Harris, J. Hylen, A. Para, NuMI-B-783, "Proposal for Continuosly-Variable Beam Energy".

[6] J. Hylen, MINOS-doc-1303, "Calibration of NuMI horn current readout".

[7] A. Marino, CC Phone Meeting, "Current Distribution in Horns: First Thoughts on Analytic Approach."

[8] R.Zwaska, talk presented at CC/ND/Beam Phone meeting July 13, 2005: http://www.hep.utexas.edu/numi/beamMC/meetings/zwaska-071305.pdf

[9] S. Kopp, M. Kostin, R. Zwaska, NuMI-B-768, "Hadron Production Models, Revisited".

[10] M. Messier *et al.*, NuMI-B-700, "Neutrino Fluxes and the Hadron Hose".

[11] J. Hylen *et al*, "Proposal to Include the Hadron Hose in the NuMI Beam", NuMI-B-542.